



DIPLOMARBEIT

Electron and Hole Wavefunctions in Andreev Billiards

ausgeführt am
Institut für Theoretische Physik
der Technischen Universität Wien

unter der Anleitung von
O.Univ.-Prof. Dipl.-Phys. Dr. Joachim Burgdörfer
und
Univ.Ass. Dipl.-Ing. Dr. Stefan Rotter

durch
Florian Libisch
Dannebergpl. 15/9
1030 Wien

Datum

Unterschrift

Contents

1	Introduction	1
2	Andreev billiards	3
2.1	Superconductivity	3
2.1.1	Ballistic motion	3
2.1.2	BCS theory	4
2.1.3	Bogoliubov-de Gennes equation	6
2.1.4	Andreev reflection	6
2.2	Quantum mechanical solution	8
2.2.1	Model system	8
2.2.2	Energy levels	9
2.2.3	Modular recursive Green's function method	11
2.2.4	Wavefunctions	12
2.3	Semiclassical treatment	14
2.3.1	Path-Length Distribution	14
2.3.2	Bohr-Sommerfeld approximation	16
2.4	Rectangular billiard	18
2.4.1	State counting function	18
2.4.2	Wavefunctions	19
2.4.3	Quantization condition	20
2.4.4	Billiard with narrow leads	22
2.5	Circular billiard	24
2.5.1	Wavefunctions	25
3	Billiard with soft walls	28
3.0.2	Quantum mechanical treatment	28
3.0.3	Semiclassical treatment	30
3.0.4	Results	31

4	Magnetic field	35
4.0.5	Implementation of a magnetic field	35
4.0.6	Low magnetic field region	37
4.0.7	Semiclassical description	38
4.0.8	High magnetic field region	42
5	Potential barrier at the SN interface	45
5.0.9	Quantum mechanical treatment	45
6	Summary and Outlook	51
A	Derivation of SN reflection phase	53
A.1	Clean SN interface	53
A.2	Potential barrier at the SN interface	55
B	Semiclassical eigenenergies	56
	Acknowledgements	61

Chapter 1

Introduction

Ballistic mesoscopic devices in two dimensions have become popular systems to investigate a wide variety of physical effects, both experimentally [1][2] as well as theoretically [3][4]. Ballistic in this context means that the mean free path of an electron is much larger than the size of the so-called quantum dots. In this regime, phase coherent scattering occurs. By combining GaAs/GaAlAs heterostructures, it is nowadays possible to confine electrons to a two dimensional electron gas with mean free paths up to $10\mu\text{m}$ [5][6]. The aim of this thesis is to investigate the dynamics when such a quantum dot is brought in contact with a superconductor.

Superconductivity was discovered by Kamerlingh Onnes in 1911. Performing experiments on mercury, he found that its resistance abruptly dropped to zero below 4.2K. A satisfactory explanation for this phenomenon was not found before 1957, when Bardeen, Cooper and Schrieffer (BCS) developed a theory [7], which states that for sufficiently low temperatures, electrons form bound pairs, so called Cooper pairs. These pairs form the so-called BCS ground state, which has a slightly lower energy than the normal Fermi sphere. The attractive force between the two equally charged electrons is due to electron-phonon coupling.

One of the most prominent features of superconductivity are the vanishing of resistance and the Meissner Ochsensfeld effect [8]. What we are interested in in this thesis is the effect a superconductor has on a normal conducting quantum dot when brought into contact with it. A ballistic normal metal coupled to a superconductor is commonly called an Andreev billiard [9][10][11]. Electron and hole excitation, which are decoupled in a normal conducting ballistic metal, become connected through the superconductor. The dynamics of the quantum dot change dramatically, because a new class of periodic orbits in the billiard is created. The reason for this is that an electron hitting the surface of a superconductor will excite another electron to form a Cooper

pair. This pair continues its path into the superconductor, leaving back a hole excitation. This phenomenon is called Andreev reflection. In case of sufficiently small excitations and the absence of diffractive effects, the hole almost exactly retraces the path of the electron, thereby creating a periodic orbit in the Andreev billiard.

A characteristic quantity in an Andreev billiard is the state counting function (i.e. the integrated density of states), which has been studied by many authors [12][13][14]. The density of states in an Andreev billiard has singularities, which results in a distinct cusps structure in the counting function [9]. As will be shown, these cusps are due to the retracing property of Andreev orbits and vanish as soon as retracing is perturbed.

Using the retracing properties of Andreev reflection, it is possible to describe very accurately the density of states of a closed Andreev billiard with a simple semiclassical formula [15]. We will try to explain why the semiclassical description of Andreev billiards is so simple and, at the same time, correct.

The outline of this thesis is as follows: First, we will give an introduction to the physics of Andreev billiards, and the methods used to simulate their dynamics. We present the conventional Bohr-Sommerfeld description of an Andreev billiard, and compare the results to the quantum mechanical calculations. We do this by not only looking at the state counting function, but at the quantum mechanical wavefunctions of these states themselves. The modular recursive Green's function method [16] we use allows us to calculate the wavefunctions of Andreev states in the normal and superconducting part of the Andreev billiard with high accuracy. To our knowledge, this has not been done before.

By looking at the limit of a narrow superconducting lead connected to comparatively large cavities, we show that for these systems retracing does not take place. This does not depend on the mean free path or the cleanliness of the SN interface, but is a consequence of the long trajectories arising for small leads.

To investigate this more thoroughly, we analyze the limits of the retracing approximation. To do this, we introduce several effects to perturb the ideal retracing conditions: A magnetic field, soft billiard walls and a potential barrier at the SN interface. We attempt to give a semiclassical approach for these cases, and show its limitations.

We finally analyze how the wavefunctions and the counting function change under the influence of these perturbations. As will be shown, the ratio of hole displacement and Fermi wavelength is a good indicator for the validity of the retracing approximation.

Chapter 2

Andreev billiards

2.1 Superconductivity

2.1.1 Ballistic motion

As mentioned in the introduction, we attempt to describe a ballistic scattering system which consists of a normal and a superconducting region. For a realistic device, this means that the mean free path of the electron is much larger than the system size. For our theoretical description, we assume inelastic scattering sources to be completely absent.

We start out by taking a look at the properties of a current carrying electron in a normal metal. Such a valence electron is subject to a periodic potential created by the crystal lattice. In general, its dispersion relation will be determined by the crystal band structure. Near a critical point k_c , the first derivative of the dispersion relation $E(\mathbf{k})$ vanishes. Assuming a simple cubic lattice, we can Taylor expand the dispersion relation around k_c [17]:

$$\begin{aligned} E(\mathbf{k}) &= E(\mathbf{k}_c) + \frac{1}{2} \frac{\partial^2 E(\mathbf{k})}{\partial k^2} \Big|_{\mathbf{k}=\mathbf{k}_c} (\mathbf{k} - \mathbf{k}_c)^2 + O((k - k_c)^3) \\ &\approx E_0 + \frac{1}{2m_{\text{eff}}} (k - k_c)^2. \end{aligned} \quad (2.1)$$

The resulting dispersion relation is shown in Figure (2.2,*a*). Introducing the effective mass m_{eff} , we note that it is possible to describe the dynamics of an electron moving through the periodic potential of a lattice near the Fermi edge with a free electron dispersion relation.

At very low temperatures, the valence electrons of the solid will form a Fermi sea as shown in Figure (2.1, *a*). All states up to the Fermi energy E_F are occupied by electrons due to the Pauli principle. If an electron is excited

by an energy ε , it moves to a higher energy, and leaves back an unoccupied state below the Fermi edge, a hole, as shown in Figure (2.1, *b*).

Imagine an electric field applied to the electrons in Figure (2.1, *a*). The excited electron can move under the influence of the field, but the other ones cannot, because their nearest states are already occupied. Only the electron next to the hole can move into the position of the hole. If it moves to the left, the hole essentially moves to the right. Thereby the hole behaves like a particle with positive charge under the influence of the field.

The dispersion relation of a hole is shown in Figure (2.2,*a*) as a dashed line. We see that the sign of the effective mass defined in Equation (2.1) is inverted. Thus, a hole does not only have opposite charge compared to the electron, but it also carries opposite effective mass.

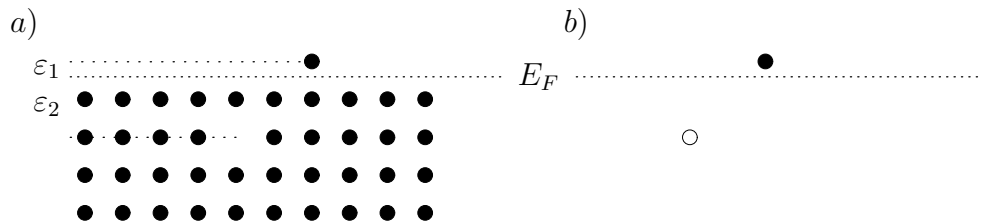


Figure 2.1: *Schematic picture of a Fermi sea of occupied electron states, one electron excitation at the energy $E_F + \varepsilon_1$ and one free position at the energy $E_F - \varepsilon_2$ (a). In the quasiparticle picture (b), there is an electron excitation with energy ε_1 and a hole excitation with energy ε_2 .*

For convenience, we use rescaled units throughout this work. We set the quantities $|e| = m_{\text{eff}} = \hbar = 1$ and dimensionless.

2.1.2 BCS theory

As mentioned in the introduction, the main breakthrough in explaining superconductivity was the concept of a Cooper pair. Under special conditions, electron-phonon interaction gives rise to an attractive force between two electrons. The exact treatment of electron-phonon interaction is quite complicated. Therefore, several approximations are made to simplify the theoretical description of superconductors.

The most prominent approximation certainly constitutes BCS theory by Bardeen, Cooper and Schrieffer [7], which describes the electron-electron coupling by introducing a constant weakly attractive force $-V_{\text{BCS}}$ for electrons near the Fermi edge. This crude approximation is sufficient to successfully

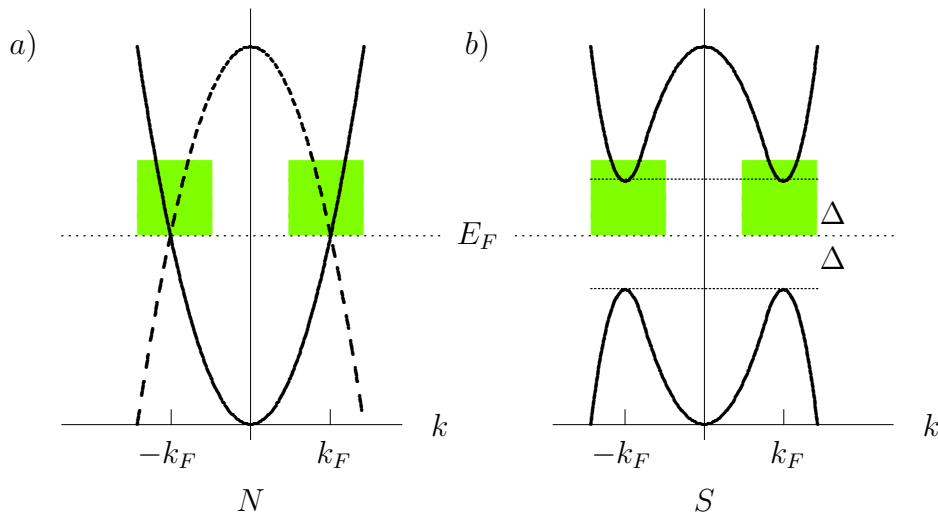


Figure 2.2: Schematic plot of excitation energies E vs wavenumber k along an axis passing through the center of the Fermi sphere for normal conducting metal (N , a) and superconductor (S , b) [18][19]. In the normal conductor, the hole excitation is shown as dashed line. The shaded areas are enlarged in Figure (2.3).

describe many aspects of superconductivity, like vanishing resistance and the Meissner-Ochsenfeld effect.

The effect of V_{BCS} is to create an energy gap around the Fermi energy in the dispersion relation, as shown in Figure (2.2, b). The size of this gap is 2Δ . $\Delta = |\Delta|e^{i\phi}$ is called the pair potential of the superconductor. It is the energy two electrons gain by forming a Cooper pair.

In the superconductor, there is no available state in the gap $[E_F - \Delta, E_F + \Delta]$ due to Cooper pair formation, as shown in Figure (2.2,b). Thus, inelastic scattering is not possible as long as the excitation energy lies below 2Δ . As a consequence, resistance drops to zero as long as thermal excitations lie below the gap, i.e. $k_B T < \Delta$. The solid becomes superconducting.

The spatial dependence of Δ is determined by [20]:

$$\Delta(\mathbf{x}) := -V_{\text{BCS}}(\mathbf{x}) \sum_{\varepsilon > 0} v^*(\mathbf{x})u(\mathbf{x})(1 - 2f(\varepsilon)) \quad (2.2)$$

where the sum includes all states with positive ε . $f(\varepsilon)$ is the Fermi function, u and v denote the electron and hole wavefunctions inside the superconductor.

Inside a superconductor, at some distance from the surface, V_{BCS} is constant and Δ assumes its bulk value $|\Delta_0|e^{i\phi}$. At the surface of the superconductor $V_{\text{BCS}}(x)$ drops abruptly to zero. Then, the exact shape of Δ has to be determined using Equation (2.2).

Equation (2.2) is a self consistency relation: The exact value of Δ depends on the wavefunctions u and v inside the superconductor. These wavefunctions, in turn, depend on Δ . To avoid the complications of solving (2.2), we assume that the length scale at which Δ drops from its bulk value to zero is much smaller than the system size. Under these assumption, a step function model for Δ is plausible [20]

$$\Delta = |\Delta_0|e^{i\phi}\theta(x - x_{SN}) \quad (2.3)$$

where x_{SN} is the position of the superconductor-normal conductor (SN) interface.

2.1.3 Bogoliubov-de Gennes equation

An elegant way to describe a superconductor-normal conductor system is the Bogoliubov-de Gennes equation. It consists of a linear expansion of the exact equations of motions of electron and hole excitations. They are coupled by the pair potential Δ introduced by the BCS theory. Writing the Schrödinger equations for electron and hole excitation as one matrix equation, we obtain the Bogoliubov-de Gennes equation [21]

$$\begin{pmatrix} H_0 & \Delta \\ \Delta^* & -H_0^* \end{pmatrix} \begin{pmatrix} u(\mathbf{x}) \\ v(\mathbf{x}) \end{pmatrix} = \varepsilon \begin{pmatrix} u(\mathbf{x}) \\ v(\mathbf{x}) \end{pmatrix}. \quad (2.4)$$

H_0 is the Hamiltonian of an electron in a potential with respect to the Fermi energy:

$$H_0 = \frac{1}{2m_{\text{eff}}}\mathbf{p}^2 + V(\mathbf{x}) - E_F. \quad (2.5)$$

By subtracting E_F from H_0 , ε is the excitation energy of an electron (hole) over (below) the Fermi energy E_F . $V(\mathbf{x})$ is an additional confining potential.

Note that the off-diagonal term in the matrix Hamiltonian in Equation (2.4) represents the coupling between electron and hole. The electron and hole wavefunctions u and v are coupled to each other by the pair potential Δ in the superconductor, and because of Equation (2.3) decoupled in the normal conductor. In such a way, the superconductor connects electron and hole dynamics of the normal conducting quantum dot.

2.1.4 Andreev reflection

The mechanism of Andreev reflection was explained by Andreev in 1964 [22]. It occurs when an electron moving inside the normal conducting quantum

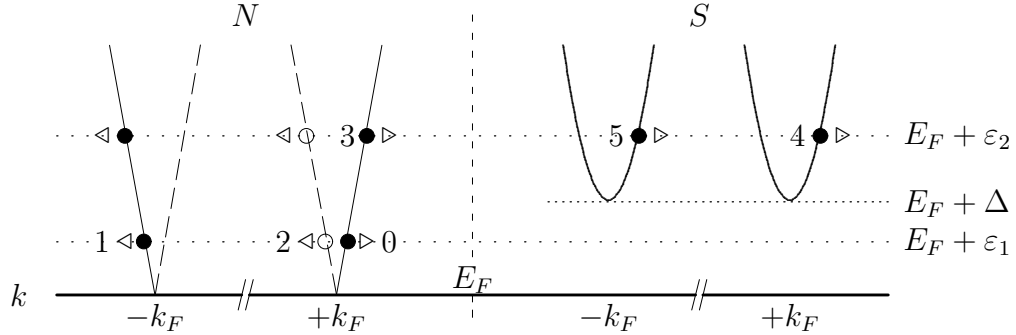


Figure 2.3: Schematic diagram of energy E vs wavenumber k at an interface between a normal conducting metal (N) and a superconductor (S), enlarged near the Fermi edge (the shaded areas in Figure (2.2)) [18]. Open circles denote holes, closed circles electrons. The small triangles indicate the directions of motion. An electron hitting the superconductor below the gap (0) with an excitation energy $\varepsilon_1 < \Delta$ will be reflected back (as there is no state in the superconductor to accommodate it) either as electron (1), or as hole (2). If the energy of the electron $\varepsilon_2 > \Delta$ lies above the gap (3), it can penetrate into the superconductor by normal (4) or Andreev (5) transmission.

dot with a small excitation energy ε above the Fermi energy E_F hits a superconductor - normal conductor (SN) boundary. Small in this context means $\varepsilon < \Delta$, as depicted in Figure (2.3). By exciting another electron, the electron forms a Cooper pair which continues into the superconductor. This second electron leaves a hole excitation with energy ε below the Fermi energy as shown in Figure (2.4). The hole is reflected back into the normal conductor, due to momentum conservation. If the electron energy is sufficiently close to the gap, the dispersion relation can be linearized close to the Fermi level. Then, the reflected hole has the opposite velocity of the electron.

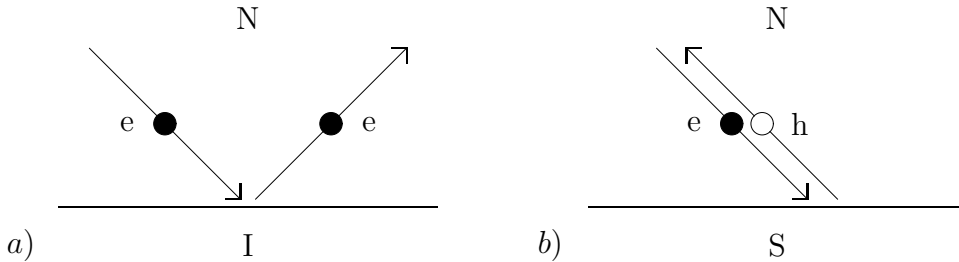


Figure 2.4: a) Normal reflection by an insulator (I) versus b) Andreev reflection by a superconductor (S) of an electron with a small excitation energy ε above the Fermi energy E_F . Andreev reflection conserves momentum, as the hole has negative effective mass. The missing charge of $2e$ continues into the superconductor as a Cooper pair.[20]

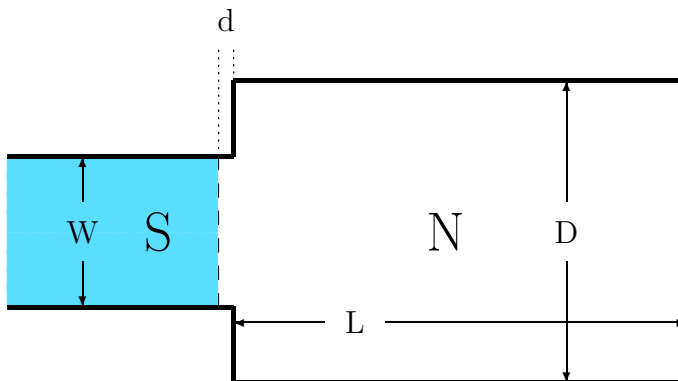


Figure 2.5: *Rectangular Andreev billiard.*

If the pair potential Δ of the superconductor and the excitation energy $\varepsilon < \Delta$, is small compared to the Fermi energy, $\Delta \ll E_F$, the energy difference between electron and hole is minimal. In this case, the hole retraces the path of the electron, until it hits the SN interface again. In such a way, a periodic orbit is formed. Any trajectory connecting the SN interface with itself will create such a periodic orbit. This feature has a major impact on the dynamics of an Andreev billiard.

To calculate the probability for Andreev reflection, we consider the above situation quantitatively. We make the ansatz of an incoming electron plane wave hitting the SN boundary. Making an ansatz of a reflected electron and hole wave, one can derive the corresponding reflection amplitudes [18]. As we consider a bound system, i.e. $\varepsilon < \Delta$, with no barrier at the SN interface, the probability for Andreev reflection is 1. For our system, this probability does not depend on the angle of the incoming wave [23]. By looking at the phase of the reflection coefficient (see Appendix A.1) of the hole, one can derive the phase difference between electron and emitted hole:

$$\delta\phi \approx -\arccos\left(\frac{\varepsilon}{\Delta}\right) \quad (2.6)$$

We will need this result for the semiclassical description of Andreev reflection.

2.2 Quantum mechanical solution

In the following, we give a short description of the methods used to calculate the energy levels and wavefunctions presented in this work.

2.2.1 Model system

We consider a bound state problem, i.e. we want to find eigenenergies $\varepsilon \leq \Delta$ of the Bogoliubov-de Gennes (B-dG) Equation (2.4). If not stated otherwise,

we choose a pair potential $\Delta = 0.02E_F$, which makes the maximal energy difference between electron and hole sufficiently small to allow for retracing. Our model system is a rectangular cavity with width D and length L as displayed in Figure (2.5). Attached on one side is a waveguide of width W and infinite length. The waveguide becomes superconducting after a distance d , which is small compared to the size of the system. We need a small length of normal conducting lead to expand the wavefunction of the normal conducting region in eigenstates of the lead near the SN interface. Technically, we assume that d is very small compared to the size of the system. The SN interface, i.e. the contact between normal conductor and superconductor, is located at $x_{SN} = 0$ to simplify calculations. We assume hard-wall boundary conditions, i.e. $V(x, y)$ is zero inside the dot and the lead and infinitely high elsewhere.

This system is described by the B-dG equation (2.4) where Δ is the pair potential, chosen to be $\Delta = e^{i\phi}\Delta_0$ inside the superconducting region (S) and $\Delta = 0$ inside the normal one (N). As we only consider one superconducting lead in this work, we can set the phase $\phi = 0$ [9]. The reason for this is that a constant ϕ only changes the overall phase of the electron and hole wavefunctions, which is without physical meaning.

2.2.2 Energy levels

At the SN interface, the solutions of (2.4) in the normal conducting part of the lead can be written as a superposition of plane waves describing left- and rightmoving electrons (with energy $E_F + \varepsilon$) and holes (with energy $E_F - \varepsilon$). In the superconducting part of the lead, the general solution is an exponentially decaying wave [9]. Electron and hole are coupled in the superconductor and separate in the normal conductor. The y -dependent part of the wavefunctions is described by $\chi_n(y)$ both in the normal- and superconducting lead. In the absence of a magnetic field, $\chi_n(y) \propto \sin(n\pi y/W)$ where the integer n denotes the index of the vertical quantization. The normalization factor is chosen such that the wavefunctions are flux-normalized. We will consider what changes if a magnetic field is switched on in Chapter 4.

Using the abbreviation $\gamma = \Delta/(\varepsilon + i\sqrt{\Delta^2 - \varepsilon^2})$ we have

$$\psi_N(\mathbf{x}) = \sum_n \chi_n(y) \left[(c_{e,n}^+ e^{ik_n^e x} + c_{e,n}^- e^{-ik_n^e x}) \begin{pmatrix} 1 \\ 0 \end{pmatrix} + (c_{h,n}^+ e^{ik_n^h x} + c_{h,n}^- e^{-ik_n^h x}) \begin{pmatrix} 0 \\ 1 \end{pmatrix} \right] \quad (2.7)$$

$$\psi_S(\mathbf{x}) = \sum_n \chi_n(y) \left[b_n^- e^{-iq_n^- x} \begin{pmatrix} \gamma \\ 1 \end{pmatrix} + b_n^+ e^{iq_n^+ x} \begin{pmatrix} \gamma^* \\ 1 \end{pmatrix} \right] \quad (2.8)$$

We want ψ_N and ψ_S to be eigenfunctions of the B-dG equation (2.4) in the normal and superconducting region. From this it follows that

$$k^{e,h} = \sqrt{2(E_F \pm \varepsilon) - k_{yn}^2} \quad (2.9)$$

$$q^\pm = \sqrt{2(E_F \mp i\sqrt{\Delta^2 - \varepsilon^2}) - k_{yn}^2}. \quad (2.10)$$

Note that the imaginary part of $\pm q^\pm$ will always be negative, resulting in an evanescent suppression of the wavefunctions in the superconducting region. However, in contrast to a normal conducting and classically forbidden region, the wavefunction still oscillates, as the wavenumber is complex, not purely imaginary.

The scattering matrix of the normal conducting open structure connects the coefficient vectors c_e^\pm and c_h^\pm :

$$c_e^- = S(\varepsilon)c_e^+ \quad , \quad c_h^+ = S^*(-\varepsilon)c_h^- \quad (2.11)$$

Furthermore, the wavefunctions must fulfill matching conditions at the SN interface:

$$\psi_S(0, y) = \psi_N(0, y) \quad (2.12)$$

$$\partial_x \psi_S(x, y)|_{x=0} = \partial_x \psi_N(x, y)|_{x=0} \quad (2.13)$$

The transverse lead eigenfunctions $\chi_n(y)$ are linearly independent and fulfill an orthogonality relation. By inserting (2.7) and (2.8) into (2.11–2.13), multiplying with $\chi_m(y)$ and integrating over y , it is thus possible to rewrite the matching conditions as linearly independent equations. Assuming a total number N of open modes in the lead, this gives us $6N$ equations for the $6N$ coefficients $c_{e,h}^\pm$ (N for each of the two (2.11) and $4N$ from electron and hole part of both (2.12) and (2.13)). After inserting Equation (2.11) to eliminate the $2N$ variables c_e^- and c_h^+ , we can write the above equations as a homogeneous matrix equation of dimension $4N \times 4N$:

$$\begin{pmatrix} \mathbb{1} + S(\varepsilon) & 0 & -\gamma_e \mathbb{1} & -\gamma_h \mathbb{1} \\ 0 & \mathbb{1} + S^*(-\varepsilon) & -\mathbb{1} & -\mathbb{1} \\ iK^e(\mathbb{1} - S(\varepsilon)) & 0 & i\gamma_e Q^e & -i\gamma_h Q^h \\ 0 & iK^h(S^*(-\varepsilon) - \mathbb{1}) & iQ^e & -iQ^h \end{pmatrix} \begin{pmatrix} c_e^+ \\ c_h^- \\ b^+ \\ b^- \end{pmatrix} = 0. \quad (2.14)$$

$K^{e,h}$ and $Q^{e,h}$ are the diagonal matrices of the wavevectors in the normal and superconducting region.

In order for an Andreev level to exist, we have to find a real ε so that the determinant of the matrix in Equation (2.14) becomes zero. As the matrix

is complex and non-Hermitian, we used a singular value decomposition to determine the ε for which it becomes singular. We can write any quadratic matrix A as

$$A = U\Sigma V^\dagger \quad U^\dagger U = V^\dagger V = \mathbb{1} \quad \Sigma = \text{diag}(\sigma_i), \quad \sigma_i \in \mathbb{R}^+. \quad (2.15)$$

The positive definite σ_i are the singular values of the matrix. If, and only if, one of them is zero, the matrix is singular. Plotting the smallest σ_i as a function of ε , we find distinct zeros representing allowed eigenvalues ε of (2.4).

It is worth noting that the only information about the shape of the cavity in Equation (2.14) enters via the scattering matrix $S(\varepsilon)$ of the open normal conducting system.

2.2.3 Modular recursive Green's function method

We will use the modular recursive Green's function method [16],[24] to calculate the scattering matrix $S(\varepsilon)$ and the wave functions inside the normal conducting rectangular quantum dot. It is important to understand that the scattering matrix is that of an open, normal conducting system, i.e. the lead in Figure (2.5) is replaced by a normal conducting one. A short description of how this method is applicable to our problem is given in the following.

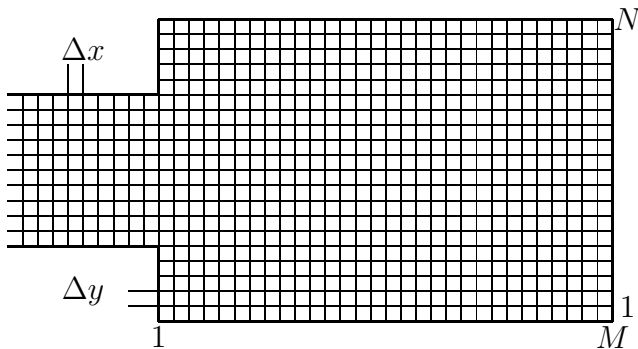


Figure 2.6: *Discretization grid on rectangular quantum dot*

To solve the scattering problem through the rectangular quantum dot numerically, we use a tight binding grid in the continuum limit. To this end, we use a tight binding Hamiltonian

$$H = \sum_j \varepsilon_j |j\rangle \langle j| + \sum_{j,k} V_{j,k} |j\rangle \langle k|. \quad (2.16)$$

The site energy ε_j and the hopping potential $V_{i,j}$ representing nearest-neighbor coupling are chosen such that the Schrödinger equation on the grid converges

towards the continuum equation in the limit of an infinitely fine grid [24]. The grid is shown in Figure (2.6). The spacing between grid points is Δx and Δy , there are $M \times N$ gridpoints in the rectangle. The grid has to be fine enough to allow for

$$1 - \cos(k_F \Delta x) \approx \frac{1}{2}(k_F \Delta x)^2 \quad (2.17)$$

in order to get the free particle dispersion relation $E = k^2/2$ from the dispersion relation on the finite sized grid, $E = 1 - \cos(k\Delta x)$.

One main idea of the modular recursive Green's function method is to separate the tight-binding grid into separable substructures, so called modules. In our case, the scattering geometry is composed of the rectangle itself and one semi-infinite wave guide. The Green's function of the rectangle is calculated by an eigenfunction expansion of the eigenfunctions of (2.16),

$$G_0(\mathbf{x}, \mathbf{x}', E) = \sum_m \frac{\phi_{[m]}(\mathbf{x})\phi_{[m]}^*(\mathbf{x}')}{E - E_m + i\eta}. \quad (2.18)$$

The Green's functions of the different modules are then put together by a Dyson equation

$$G = G_0 + G_0 V G \quad (2.19)$$

to assemble the Green's function of the complete structure.

The scattering wave functions ψ_m^+ inside the cavity can now be expressed by projecting the retarded Green's function of the structure onto the incoming wave [25],

$$\psi_m^+(\mathbf{x}) = -\sqrt{k_{x,m}} \int_0^W dy' G^+(\mathbf{x}, \mathbf{x}', E) \chi_m(y')|_{x'=0}, \quad (2.20)$$

2.2.4 Wavefunctions

With the help of Equation (2.20), we can calculate the wavefunctions inside the normal conductor using the Green's function. After determining an ε by (2.14), we need to find a nontrivial eigenvector to the eigenvalue zero of the singular matrix. Numerically, this is not a simple problem, as the usual approaches for solving linear equation, e.g. matrix inversions, fail. We use the singular value decomposition (2.15). As V^\dagger is a unitary matrix, its columns form an orthonormalized complete basis. The column of V^\dagger corresponding to $\sigma = 0$ contains the normalized eigenvector we are looking for. Thus, we can write the electron wavefunction in the normal conductor as

$$u_N(\mathbf{x}) = -\sum_n \sqrt{k_n^e} c_{e,n}^+ \int_0^W dy' G^+(\mathbf{x}, \mathbf{x}', E) \chi_n(y')|_{x'=0}, \quad (2.21)$$

and for the hole

$$v_N(\mathbf{x}) = - \sum_n \sqrt{k_n^h} c_{h,n}^- \int_0^W dy' G^+(\mathbf{x}, \mathbf{x}', E) \chi_n(y')|_{x'=0}. \quad (2.22)$$

To calculate the exponential tail in the superconducting region, we use Equation (2.8) with coefficients b_n^\pm . Note that while the wavefunction in the superconductor is given as a sum of analytically determined functions¹ in the continuum limit, the wavefunction in the normal conductor is determined numerically on a tight binding grid, as analytic solutions for a non-vanishing difference between the width D of the rectangular cavity and the width W of the superconducting lead do not exist. In spite of these two very different approaches, we were able to fulfill the matching conditions (2.12, 2.13) with great accuracy. This shows that the grid was fine enough for the continuum limit.

Finally, the wavefunctions are normalized according to

$$\iint (|u|^2 + |v|^2) d\mathbf{x} = 1 \quad (2.23)$$

where the integral extends over the normal conducting region and the superconducting lead. The probability to find the excitation either as an electron or as a hole anywhere is one. Figure (2.7) shows an example of the calculated wavefunctions.



Figure 2.7: *Absolute square of the electron (left, $|u|^2$) and hole (right, $|v|^2$) wavefunctions calculated for a quadratic Andreev billiard (linear dimension $D = 1$, attached to a lead with width $W = 0.8$). $k_F = n_y * \pi / W = 21.5 * \pi / 0.8$, where $[n_y]$ is the number of open modes in the lead. Shown are false color plots, black areas represent zero amplitude, red the highest. The state shown has an excitation energy of $\varepsilon = 0.558\Delta$*

¹although the coefficients have to be determined numerically

2.3 Semiclassical treatment

One interesting feature of Andreev billiards is that already an elementary semiclassical description based on the Bohr-Sommerfeld quantization rule for periodic orbits leads to very accurate predictions of e.g. the state counting function [26]. Quite in contrast, great effort must be taken to find a reasonably accurate semiclassical description of normal conducting systems where no superconducting walls are present, by including e.g. the introduction of diffractive effects [27][28]. The standard approximation made to describe Andreev billiards semiclassically is to assume exact retracing of electron and hole trajectories [15], [20]. With this approach and [26] we will derive a semiclassical expression for the state counting function $N(\varepsilon)$, i.e. the number of energy levels lying below the energy ε .

2.3.1 Path-Length Distribution

For a semiclassical treatment of Andreev billiards we need the periodic orbit length distribution $P(s)$, where s denotes the length of the electron (or hole) trajectory. Because of the creation of periodic orbits by Andreev reflection, $P(s)$ corresponds to the classical pathlength distribution of the normal conducting cavity, i.e. the probability that classical electrons entering the cavity with an angular distribution of $\cos(\theta)$ exit after a pathlength of s . It is normalized to one: $\int P(s)ds = 1$.

Any trajectory connecting the SN interface with itself will automatically represent a closed periodic orbit due to retracing as shown in Figure (2.8). Thus, there is a continuum of periodic orbits formed by Andreev reflection. We do not have to search for trajectories where the electron after transversing the cavity exactly returns to the place it started from.

In the case of a rectangular cavity with one entire side replaced by a superconductor, there is an analytic expression for $P(s)$ [9]. Consider the extended zone scheme as shown in Figure (2.8,b). Every path leaving the entrance with an angle ϑ has a length $s = 2L/\cos\vartheta$. As a simple approximation, we assume that the angular distribution of the different paths is described classically by a cosine. This is a good approximation for more than 10 open modes in the lead².

$$P(\vartheta)d\vartheta = \cos(\vartheta)d\vartheta = \cos(\vartheta)\frac{\cos(\vartheta)^2}{2d\sin(\vartheta)}ds = \frac{4d^2}{s^3\sqrt{1 - \left(\frac{2d}{s}\right)^2}}ds$$

²More complicated calculations using Fraunhofer diffraction lead to different angular distributions for the different transverse modes [29]. A sum over all open modes reproduces the cosine distribution.

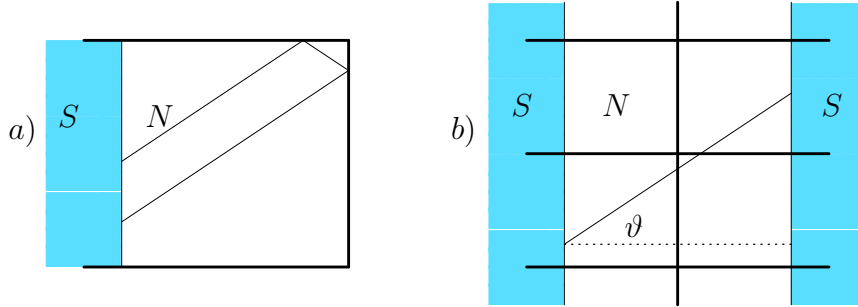


Figure 2.8: a) Quadratic ($D = L$) quantum dot with one side replaced by a superconductor ($W = D$). The trajectory shown forms a closed Andreev loop containing two Andreev reflections. b) shows the same trajectory in the extended zone scheme (scaled down by a factor of two). By arranging multiple billiards next to each other, any trajectory can be drawn as straight line. The angle θ can be used to express the length s of the trajectory: $s = 2L / \cos(\vartheta)$.

For a more general shape of the cavity, numerical Monte Carlo calculations using Equation (2.32) were used to determine $P(s)$. Typically 1.500.000 trajectories with an angular distribution of $\cos(\theta)$ were employed. Figure (2.9) shows the numerical results for four different lead widths.

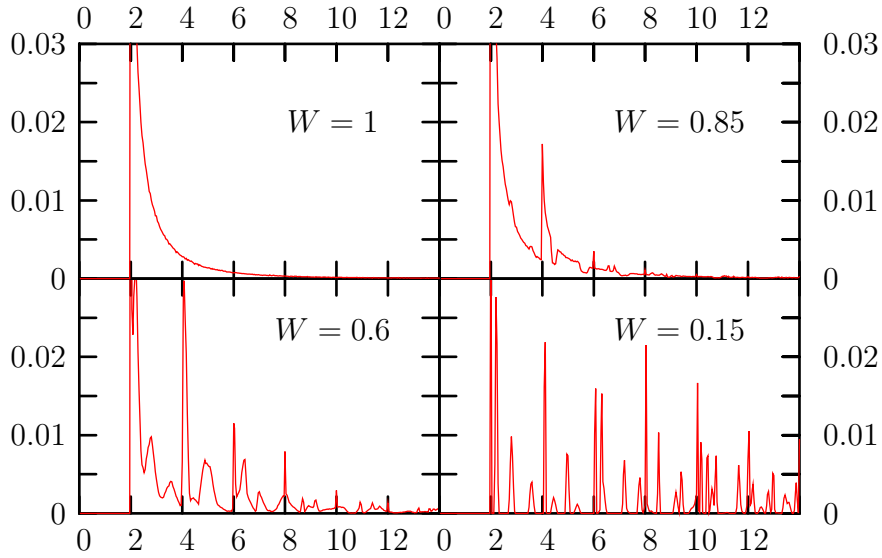


Figure 2.9: Numerically calculated $P(s)$ for different lead widths as shown in the insets in a 1×1 rectangle. The peak at $l = 2$ represents paths exiting the cavity after being reflected at the right wall once. The smaller the lead, the more complicated the structure of $P(s)$.

2.3.2 Bohr-Sommerfeld approximation

The Bohr-Sommerfeld quantization rule is a very basic quantization scheme used to describe periodic motion in the early days of quantum mechanics [30]. As periodic orbits formed by the hole retracing the path of the electron play the essential role in the dynamics of Andreev billiards, we can describe these dynamics using the Bohr-Sommerfeld approximation.

We want to derive a semiclassical prediction for the state counting function. To this end, we start out from the semiclassical density of states [26]

$$\rho_{\text{BS}}(\varepsilon) = N \int_0^\infty ds P(s) \sum_{n=0}^\infty \delta(\varepsilon - \varepsilon_n(s)) \quad (2.24)$$

where $\varepsilon_n(s)$ is chosen such that the energy level fulfils the Bohr-Sommerfeld quantization condition for the action S :

$$S = S_e - S_h = \int \mathbf{p}_e d\mathbf{q}_e - \int \mathbf{p}_h d\mathbf{q}_h = 2\pi(n + \frac{\mu}{4}) \quad (2.25)$$

where μ is the Maslov index [31], which describes phase contributions due to classical turning points, e.g. reflections at the SN interface or the hard wall boundary.

For hard walls at the border of the dot and zero potential inside, the line integral (2.25) gives the action, i.e. the length of the trajectory s times the wavenumber k . The action of the hole excitation contributes with a negative sign. We consider a periodic orbit, a trajectory of length s connecting the superconducting lead with itself.

$$S = s(k_e - k_h) = sk_F \left(\sqrt{1 + \frac{\varepsilon}{E_F}} - \sqrt{1 - \frac{\varepsilon}{E_F}} \right) \approx s \frac{2\varepsilon}{k_F}. \quad (2.26)$$

In the last step, we used a Taylor expansion of first order of the square root. The difference in energies between electron and hole is 2ε . The main part of the phase the electron accumulates while transversing the billiard is subtracted out again by the hole retracing it. Thus, the action of a periodic orbit varies much slower with the length of s than for a normal conducting system. On the other hand, this argument relies on two large quantities S_e and S_h nearly cancelling out each other and thereby giving a contribution of the order ε/k_F , which cannot be considered large compared to \hbar . However, a semiclassical approximation consists of neglecting terms of order \hbar . From this point of view, it is surprising that a semiclassical description of Andreev billiards relying on periodic orbits works as well as it does.

Additionally, there is a phase shift of $-2 \cdot \arccos(\frac{\varepsilon}{\Delta})$ due to the two Andreev reflections as we show in Appendix (A.1). We do not need to consider other reflections at the normal conducting hard wall boundary each contributing a phase jump of π , because the sum of both the electron and the hole reflection add up to a total contribution of $2n\pi$, where the integer n denotes the number of reflections. A phase shift of integer multiples of 2π is irrelevant as the phase is only defined modulo 2π . The complete phase accumulated in one closed trajectory is thus

$$\phi = \frac{2\varepsilon s}{k_F} - 2 \cdot \arccos\left(\frac{\varepsilon}{\Delta}\right). \quad (2.27)$$

According to Bohr-Sommerfeld, the above phase has to be equal to $2n\pi$, which gives

$$s_n(\varepsilon) - \left(n\pi + \arccos\left(\frac{\varepsilon}{\Delta}\right)\right) \frac{k_F}{\varepsilon} = 0. \quad (2.28)$$

Inserting this expression into Equation (2.24) we obtain

$$\rho_{BS}(\varepsilon) = N \int_0^\infty ds P(s) \sum_{n=0}^\infty \delta(s - s_n(\varepsilon)) |\partial_\varepsilon s_n(\varepsilon)|. \quad (2.29)$$

The derivative of $s_n(\varepsilon)$ appears because of the familiar formula $\delta(f(x)) = \sum_i \delta(x - x_i)/|f'(x_i)|$. The sum over i can be left out because $s_n(\varepsilon)$ is strictly monotonic in ε and thus only has one root.

To compare the results of the semiclassical approximation with quantum mechanical calculations, it is useful to consider the semiclassical state counting function

$$N_{BS}(\varepsilon) = \int_0^\varepsilon d\varepsilon' \rho_{BS}(\varepsilon') \quad (2.30)$$

$$= N \int_0^\infty ds P(s) \sum_{n=0}^\infty \int_0^\varepsilon d\varepsilon' \underbrace{\delta(s - s_n(\varepsilon'))}_{\delta(\varepsilon - \varepsilon_n)} |\partial_{\varepsilon'} s_n(\varepsilon')|. \quad (2.31)$$

Using Equation (2.28) one can perform the integral over ε' using the delta function in the following way: The integral over ε' in (2.31) equals the number of roots of $s_n(\varepsilon')$. $s_n(\varepsilon')$ is a strictly monotonically decreasing smooth function in ε . From this it follows that, for a given ε' , $s_n(\varepsilon')$ defined in Equation (2.28) is the smallest s for which the delta function in (2.31) can contribute. Furthermore, for fixed $s > s_n(\varepsilon)$, there is only one root and the integral over ε' gives 1.

$$N_{BS} = M \sum_{n=0}^\infty \int_{s_n(\varepsilon)}^\infty P(s) ds. \quad (2.32)$$

One important point to notice in Equation (2.32) is that the exact shape of the paths connecting the superconductor with itself does not enter anywhere. As discussed above, the number of reflections at the normal conducting walls are irrelevant. The entire information of the specific geometry enters via $P(s)$.

2.4 Rectangular billiard

We will now use the methods described in the previous two chapters to look more closely at the dynamics of a rectangular Andreev billiard.

2.4.1 State counting function

By inspection of Equation (2.32) and Figure (2.9), we can already get an idea about how the semiclassical approximation for the state counting function will look like. Let us first consider the simplest case of $W = 1$. $P(s)$ then has one singularity at $s = 2L$, coming from orbits that reflect only once at the right side of the rectangle. We know that $N(0) = 0$. As ε increases, $s_0(\varepsilon)$ decreases, thereby increasing $N(\varepsilon)$ faster as $P(s_0(\varepsilon))$ gets larger. As soon as s_0 reaches $2L$, the counting function stops increasing, producing a cusp. This continues for increasing ε , producing cusps whenever

$$2L\varepsilon = \left(n\pi + \arccos\left(\frac{\varepsilon}{\Delta}\right) \right) k_F. \quad (2.33)$$

Figure (2.10) shows the counting function for four different lead widths. The agreement between the semiclassical prediction and our numerical calculations is very good. The cusp structure we expect is indeed visible, and the position of the cusps is predicted correctly by the Bohr-Sommerfeld approximation. The eigenenergies of a closed quadratic cavity without superconducting lead are marked in the figure too. There is only one twofold degenerate eigenstate in the energy range $[E_F, E_F + \Delta]$, in comparison to about 25 Andreev states. This relatively high number of states is due to the new periodic orbits created by retracing.

For smaller W , $P(s)$ gets more complicated and acquires more peaks, as shown in Figure (2.9). Because of this, the cusp structure becomes washed out and less distinct as the lead becomes narrower, as shown in Figure (2.10). Due to these additional peaks in $P(s)$, additional cusps start to form: For $W \approx 0.8$, $P(s)$ shows one distinct peak at $s = 4L$. The corresponding cusp forms about halfway between zero and the main cusp and is marked with an arrow in the figure. For a lead width of $W = 0.6$, the distinct cusp structure

is already quite washed out. We will discuss what happens for still narrower leads in the next chapter.

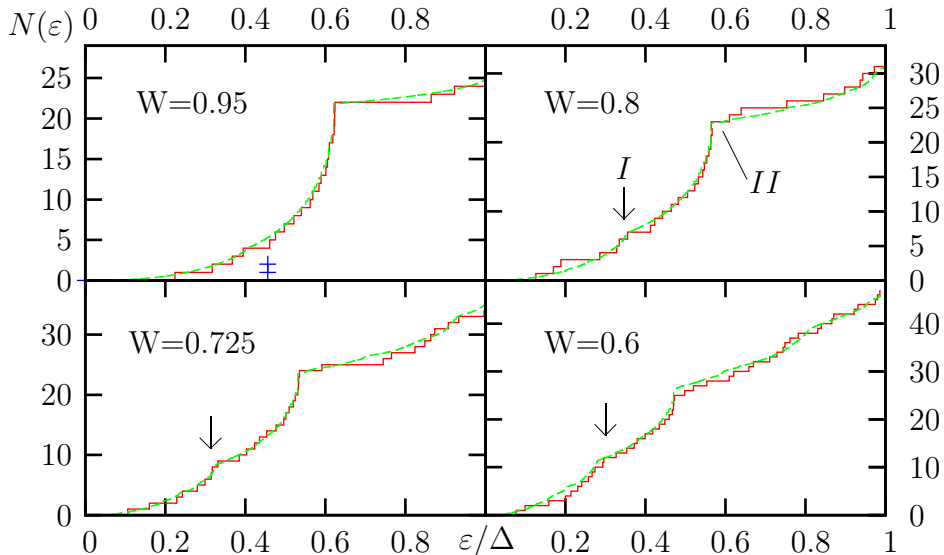


Figure 2.10: Quantum mechanical state counting function (red line) and semiclassical prediction (green dashed line) for the state counting function $N(\varepsilon)$. Shown are the results for four different lead widths W , a quadratic cavity of unit size, $k_F = 20.51\pi/W$, $\Delta = 0.02E_F$. For $W = 0.95$, the eigenenergies of the rectangular closed normal conducting billiard are marked with blue crosses. For $W \leq 0.8$, one can see the formation of a second cusp (marked with an arrow) stemming from paths with length 4. Figure (2.11) shows the electron and hole wavefunctions at the cusps marked by I and II .

2.4.2 Wavefunctions

Figure (2.11) shows examples of the corresponding wavefunctions for $W = 0.8$. The eigenstates corresponding to the two cusps marked by I and II in Figure (2.10) are shown. From the considerations in the previous section, we expect orbits of length $s = 4$ in the pictures marked a and b taken at cusp I and $s = 2$ in the pictures marked c , d and e taken at cusp II .

We can indeed see the localization of the wavefunction around the semiclassical trajectories very clearly in Figure (2.11). The path lengths expected by a semiclassical analysis are correct. From this we learn that the Bohr Sommerfeld approximation not only gives a very good prediction for the state counting function, but that the shape of the quantum mechanical eigenfunctions indeed corresponds to the expected semiclassical paths.

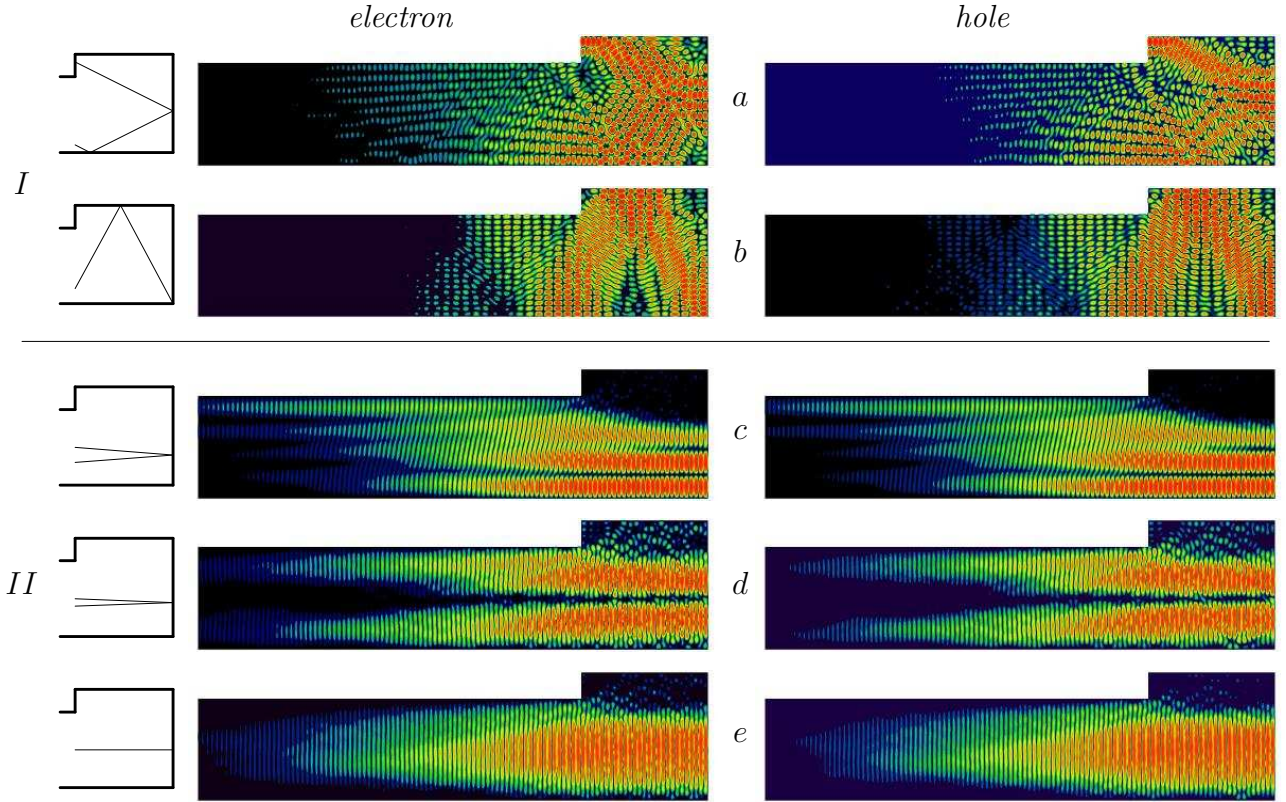


Figure 2.11: *Electron and hole wavefunctions of the states corresponding to Figure (2.10) for $W = 0.8$. Energies ε are $(0.33, 0.355, 0.563, 0.565, 0.566)\Delta$ (a-e). The corresponding semiclassical periodic orbits are shown in the insets: a and b show periodic orbits of length 4, forming part of the first small cusp (I in Figure (2.10)). c, d and e represent orbits of length 2, contributing to the main cusp marked II in Figure (2.10).*

2.4.3 Quantization condition

By looking more closely at the wavefunctions $c - e$ in Figure (2.11), one can see that as the eigenstate energies increase, the transverse quantization decreases from mode 3 in (c) to 1 in (e). This is true for the hole too, though its energy is lower in e than in c . Wavefunction e corresponding to the highest eigenenergy located at the cusp has a transverse quantum number of 1.

In order to better understand this behaviour, let us go back to the simple case of $W = D$. Quantum mechanics tells us that in the superconductor and the normal conductor the transverse component of the wavenumber will be quantized

$$\chi_n(y) = \sin(k_{ym}y) \quad , \quad k_{ym} = \frac{m\pi}{D}. \quad (2.34)$$

We use the BS quantization rule derived above, making use of the fact that $s = 2L/\cos(\theta)$ for $W = 1$, as shown in Figure (2.8). Writing $\cos(\theta) \approx \sqrt{1 - (k_{ym}/k_F)^2}$, we arrive at

$$2L\varepsilon = \left(n\pi + \arccos\left(\frac{\varepsilon}{\Delta}\right) \right) \sqrt{k_F^2 - (k_{ym})^2}. \quad (2.35)$$

This is a transcendental equation for $\varepsilon(n, m)$, which allows us to approximately calculate energy levels for $W=1$. The accuracy of these eigenenergies can greatly be improved by treating the electron and hole contribution to s separately, as shown in Appendix B.

n	m	$\varepsilon_{n,m}$ (QM)	$\varepsilon_{n,m}$ (BS) (2.35)	$\varepsilon_{n,m}$ (B-5)	Error of (B-5)
1	15	0.931	0.98	0.939	0.8%
0	1	0.747	0.75	0.746	0.1%
0	2	0.746	0.74	0.744	0.2%
0	3	0.745	0.74	0.741	0.5%
0	4	0.736	0.74	0.736	0%
0	5	0.727	0.73	0.731	0.5%
0	6	0.726	0.72	0.722	0.5%
0	7	0.708	0.71	0.712	0.6%
0	8	0.704	0.70	0.700	0.6%
0	9	0.679	0.68	0.685	0.9%
0	10	0.658	0.66	0.665	1%
0	11	0.633	0.64	0.639	0.9%
0	12	0.593	0.60	0.604	1.8%
0	13	0.555	0.56	0.552	0.5%
0	14	0.461	0.48	0.474	2.8%
0	15	0.303	0.35	0.321	6%

Figure 2.12: *The exact quantum mechanical eigenenergies (in units ε/Δ) in an Andreev billiard with $k_F = 15.51\pi$, $W = L = D = 1$. The first two columns show the quantum numbers used in Equation (2.35). The third column gives the solutions to the quantum mechanical eigenvalue problem (2.4) for this geometry. The fourth column gives the eigenenergies of the same system calculated using (2.35). As shown in appendix B, the accuracy of this equation can be improved (fifth column). The last column shows the relative error made by (B-5) with respect to the exact values.*

Table (2.12) shows the numerical results, along with the correct quantum mechanical eigenenergies. The error of the prediction is also shown in the

table. Considering that we do a semiclassical analysis, it is quite small. The clear advantage of (2.35) over the quantum mechanical calculation is that it still contains the two quantum numbers n, m , which give information about the shape of the wavefunction, i.e. the number of transverse maxima.

Equation (2.35) is sufficiently accurate as to give us an idea of the distribution of the energy eigenvalues. For fixed n and high m , the energy levels are widely spaced, as can be seen in Table (2.12). As m gets lower, the distance between adjacent energy levels shrinks until we reach $m = 1$ at $\varepsilon = 0.746\Delta$. For one fixed value of n , the number of states in one cusp is equal to the number of open modes in the cavity. We notice that the cusp contains states with low transverse quantum number m . As can well be seen in Figure (2.11), this general behaviour is still true for $W < 1$.

2.4.4 Billiard with narrow leads

If the superconducting lead attached to the normal-conducting rectangular cavity becomes very narrow, the classical pathlength distribution drops off more slowly, as shown in Figure (2.9). Longer paths must be included to correctly describe the system semiclassically. However, if the paths get longer, the approximation made by assuming perfect retracing is no longer valid. In other words: If the lead becomes too narrow, our previously employed semiclassical description breaks down.

Our aim is to find an indicator of how justified the retracing approximation is for a given lead width. Consider a trajectory connecting the SN interface with itself. The electron starts an Andreev loop at the SN interface, moves through the cavity, is Andreev reflected and then moves on as a hole. As the hole only approximately retraces the path of the electron, the hole will not hit the interface exactly at the position the electron left it, but a distance δy away. In order for dynamics to be influenced by this, δy must be of the order of the de Broglie wavelength of the electron. If δy is smaller than λ_F , the electron “does not see” that retracing is imperfect.

How large is δy for a given trajectory? After an electron with $k^2 = k_{x,e}^2 + k_y^2$ hits the SN interface, it is Andreev reflected as a hole with new $k'^2 = k_{x,h}^2 + k_y^2$. The wavenumber in y -direction is conserved. Using the wavenumbers to represent the angle of the trajectories, we get

$$\begin{aligned} \delta y &= s (\sin(\theta_h) - \sin(\theta_e)) = sk_y \left(\frac{1}{\sqrt{2(E_F - \varepsilon)}} - \frac{1}{\sqrt{2(E_F + \varepsilon)}} \right) \\ &\approx \frac{sk_y}{k_F} \frac{\varepsilon}{E_F}. \end{aligned} \tag{2.36}$$

Inserting $\varepsilon \approx \Delta/2 = 0.01E_F$, as is the case for our model system, we finally arrive at

$$\frac{\delta y}{\lambda_F} \approx \frac{sn_y}{200W}. \quad (2.37)$$

where n_y equals the number of open modes in the lead, which is 15 in the following discussion. For wide leads, $\delta y/\lambda_F$ quantity is much smaller than 1, as a result of which retracing is in this case a good approximation. In the case of $W=0.5$, however, $s \approx 6$ and $\delta y/\lambda_F \approx 1$.

To prove the validity of the above argument, we compare quantum mechanical and semiclassical results on a more quantitative level. We look at the root mean square of the difference between them:

$$\delta N = \sqrt{\frac{1}{\Delta} \int_0^\Delta d\varepsilon |N_{\text{BS}}(\varepsilon) - N_{\text{QM}}(\varepsilon)|^2}. \quad (2.38)$$

N_{QM} is the staircase function of the quantum mechanical eigenenergies

$$N_{\text{QM}}(\varepsilon) = \sum_i \theta(\varepsilon - \varepsilon_i) \quad (2.39)$$

Figure (2.13) shows δN defined in Equation (2.38) as a function of the leadwidth. As can be seen, the error generally increases with decreasing lead width. As soon as the leadwidth W reaches about one fifth of the width of the cavity D , $W = 0.2D$, semiclassical approximations relying on retracing break down. They predict a nearly linear $N(\varepsilon)$ without any discernable cusp structure. Quantum mechanical calculations on the other hand show a much lower irregular $N(\varepsilon)$, because retracing is violated and many Andreev states cease to exist. This is discussed more thoroughly in Chapter 4, Figure (4.10).

In general, we can expect the agreement between the semiclassical approximation and quantum mechanics to be better with wider leads. This has two reasons: For one, the length of the average trajectory is shorter. Shorter trajectories have less time to separate because of their different energies. Secondly, for narrow leads, diffractive effects play an important role [29]. As diffraction at the lead-opening is a random change in direction, it destroys retracing.

The influence of diffraction can be investigated by comparing different geometries. The two different geometries are shown in the inset of Figure (2.13). In one, the lead is attached at the center of the left side of the rectangular quantum dot. In the other geometry, it is attached at the bottom end of the left side. The former structure has two corners at the junction between structure and lead, the latter only one. Results show that the error is

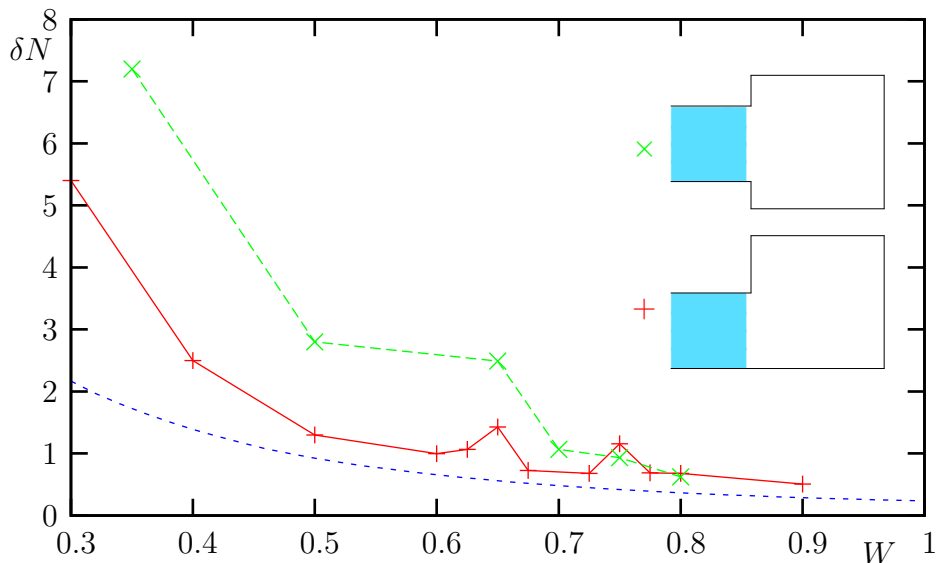


Figure 2.13: *The root mean square δN of the difference between quantum mechanical state counting function and semiclassical approximation as a function of leadwidth W for two different geometries as shown in the inset. The centered geometry (\times) has two diffractive corners at the junction between superconducting lead and rectangular cavity, thus larger disagreement with semiclassical theory is expected than in the asymmetric cavity ($+$). Generally, for decreasing lead width, the error increases. At $W = 0.15$, the semiclassical approximation breaks down completely ($\delta N \gg 10$, not shown). The value of $\delta y/\lambda_F$ is shown as a function of W as dotted purple line. It stays below 1 for $W \geq 0.5$. Its increase corresponds well with the increase in δN .*

higher in the centered case. This suggests that diffraction at the two corners might play an important role.

One additional way to determine whether retracing is active is by looking at the wavefunctions. Figure (2.15) in the next section shows wavefunctions for narrow leads.

2.5 Circular billiard

As another type of geometry with regular dynamics, we investigate the circular Andreev billiard. In our investigations, this Andreev billiard system consists of a circular cavity connected to a superconducting waveguide. The modular recursive Green's function method works by solving the Schrödinger equation in polar coordinates on a circular grid, as shown in Figure (2.14).

Due to the modular setup of this method the lead width is required to be small compared to the diameter of the circle, $W \ll 2R$.

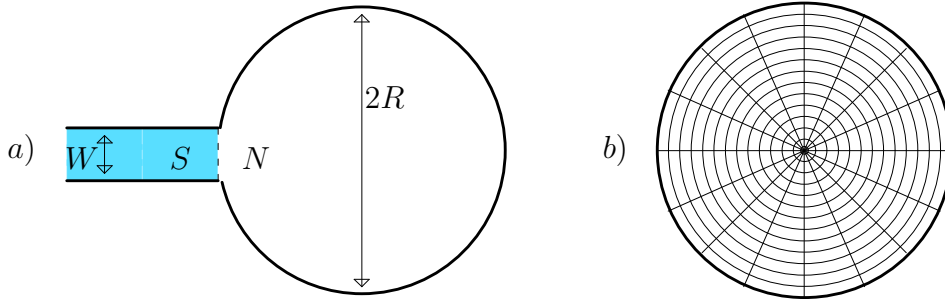


Figure 2.14: *a) Circular Andreev billiard and b) discretization grid on the circle. We use a symmetry adapted grid to discretize the Schrödinger equation.*

The wave function matching condition used to determine the Andreev eigenstates is independent of the shape of the geometry attached to the superconducting lead. The only change occurs in the calculation of the scattering matrix used in Equation (2.11).

Both the circular and the rectangular geometry are structures exhibiting regular dynamics. As a consequence, an initial angular separation between electron and hole trajectory grows linearly with the length of the trajectory. From this it follows that the estimate for $\delta y/\lambda_F$ derived in Equation (2.37) can be adapted to the circular geometry without change.

In the circular geometry considered, the average s is far greater than in a rectangular geometry. This is due to star-like trajectories hitting the wall several times, as shown in the hole part of Figure (2.15, b). Additionally, the method requires $W \ll R$ as mentioned above. We used $D = 10W$ in our calculations. As can be seen by looking at Equation (2.37), $\delta y \gg \lambda_F$, even for low energies. From this it follows that semiclassical approximations will not agree well with quantum mechanical calculations.

Indeed, the results of our semiclassical calculations did agree poorly with our quantum mechanical calculations (not shown). The discrepancies are greater than expected by taking into account long trajectories. One possible explanation for this are diffractive effects. We investigate this by calculating the wavefunctions of the Andreev eigenstates.

2.5.1 Wavefunctions

Figure (2.15) shows eigenstates of the circular Andreev billiard. We observe a great difference between electron and hole trajectory, as can be expected

if retracing is suppressed. Especially, when looking at the electron part of (2.15, *b*) we can see a very distinct localization of the wavefunction along semiclassical trajectories. However, even though we observe the electron and hole to localize around the same classical orbit in some cases, e.g. (2.15, *c*), the wavefunctions for hole and electron look quite different in the majority of the cases we investigated.

The difference between the electron and hole injection³ angle can become quite large, as in (2.15, *a*, *b*). To elucidate this, the insets show the corresponding semiclassical trajectories. The difference in energies between electron and hole is too small to allow for such differences without diffractive effects. As the electron or the hole hit the corner where the lead connects to the cavity, diffraction occurs. This is an explanation for the different angles observed in the figure.

³Insofar as we observe a closed structure, there is no injection. What we mean is the angle ϑ in Figure (2.8).

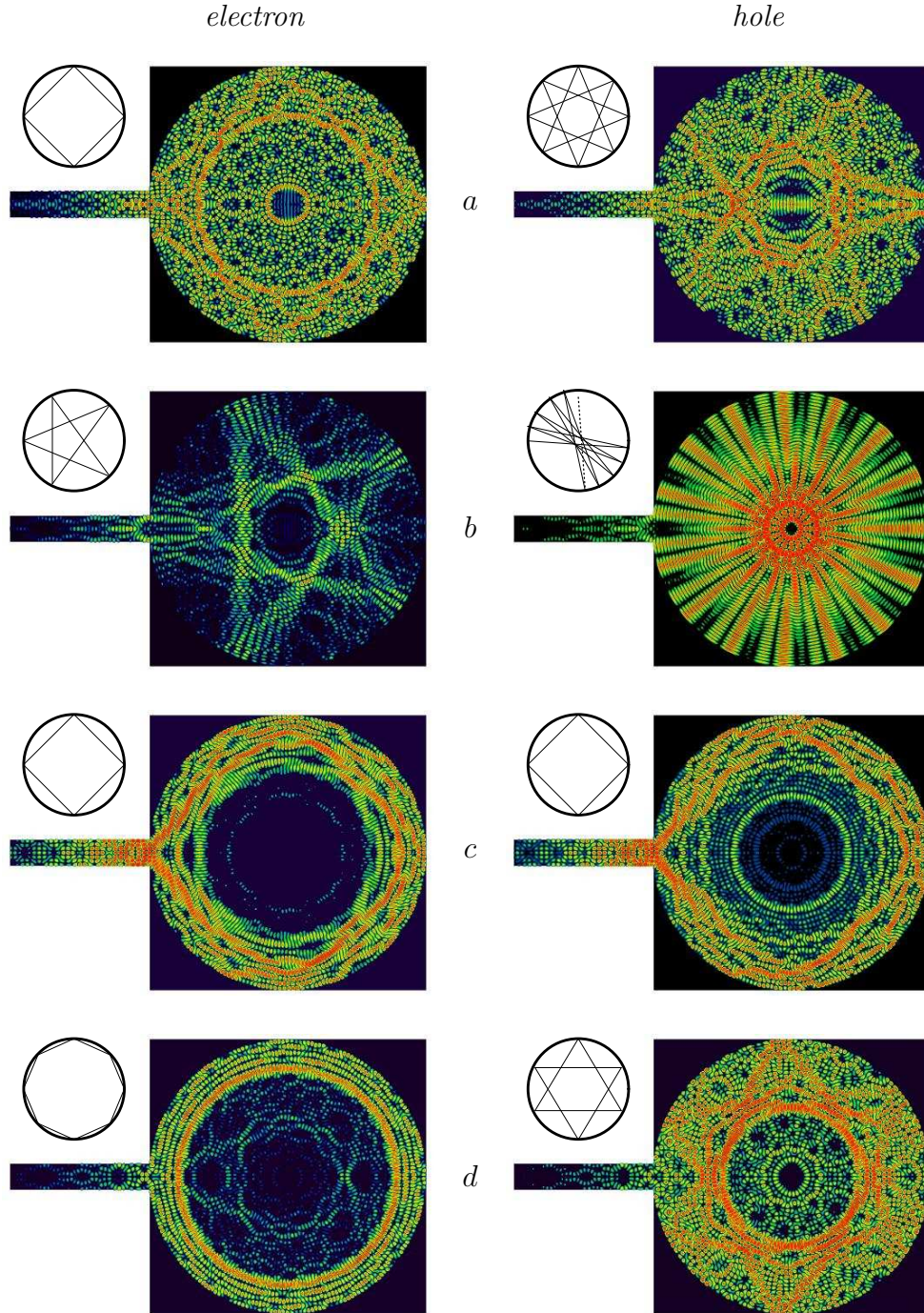


Figure 2.15: Wavefunctions of the circular Andreev billiard for eight open modes in the lead. Energies corresponding to $k_F = 8.5\pi/0.2$, $\varepsilon/\Delta = 0.23$ (a), 0.35 (b), 0.5 (c), and 0.63 (d). The diameter of the circle is 2. Clearly, retracing is violated, as the trajectories of electrons and holes shown in the insets are very different.

Chapter 3

Billiard with soft walls

In the second part of this thesis, we want to investigate retracing under non ideal conditions. One has to keep in mind that the Andreev billiards presented in the previous chapter are ideal systems. Even then, the introduction of a narrow lead is enough to offset the delicate mechanism of retracing, as we have shown. The premise of small $\Delta \ll E_F$ is not sufficient to ensure the reliability of semiclassical approximations relying on retracing.

In a realistic experimental device, several additional effects may disturb the dynamics of an ideal Andreev billiard. We mention e.g. the presence of an oxid layer at the SN contact or lattice defects giving rise to diffraction.

To investigate the role of reflections at realistic boundaries in the semiclassical description of Andreev billiards, we look at a system with soft walls. A soft wall is a much more realistic description of an experimental situation than an infinitely high potential wall. Whereas the reflection at hard walls is energy-independent semiclassically, a soft wall boundary produces energy dependent classical trajectories. We will show that for the special case of a harmonic potential the action can still be written as energy times some properly defined trajectory length, which allows us to adapt $P(s)$ to this case.

3.0.2 Quantum mechanical treatment

Figure (3.1) shows the dot we want to describe. To retain separability, we use a system with parabolic potential walls of the form

$$V(y) = \alpha E_F \left(|y| - \frac{W}{2} \right)^2 \theta(|y| - W/2) \quad (3.1)$$

and, for simplicity, hard walls parallel to the y -axis. The superconducting lead of width W is attached to the center of one of the hard walls at $x = 0$

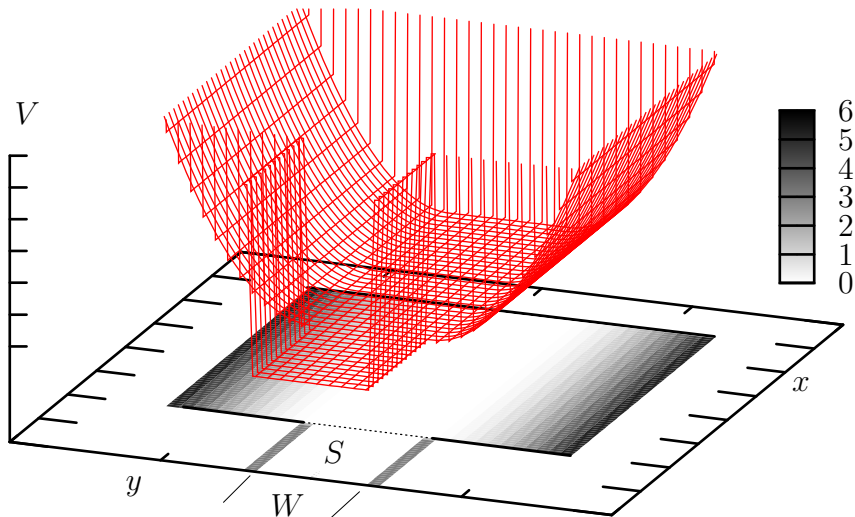


Figure 3.1: *Quantum dot with harmonic walls at the sides (arbitrary units). We choose the potential to be soft only at two opposing sides of the geometry and thereby retain the separability of the discretized Schrödinger equation.*

as shown in Figure (3.1). Because the potential is zero for $|y| < W/2$ due to the theta function in Equation (3.1), the procedure of the wave function matching at the SN interface does not change. We only have to incorporate $V(y)$ into the calculations of the scattering matrix.

The coefficient α determines the slope of the potential as a multiple of the Fermi energy. The structure is, in principle, of infinite size in y direction in contrast to the previously discussed hard wall cavity. In order to obtain in practice a finite sized cavity for the numerical calculations, we replace $V(y)$ by an infinitely high potential for $|y| \geq \tilde{D}/2$. Care must be taken to choose the cutoff-point \tilde{D} high enough that the wavefunction “does not feel” the hard wall due to the finite size of the cavity, i.e. some electron wavelengths behind the point where $V(y)$ reaches the Fermi energy [32].

Because $V(y)$ only depends on y , it is easily incorporated into the modular recursive Green’s function method. The site energies used in the tight binding Hamiltonian (2.16) are increased by $V(y_i)$. No other change in the quantum mechanical calculations of the Andreev billiard is required.

3.0.3 Semiclassical treatment

To treat an Andreev billiard with soft walls semiclassically, we use a Runge-Kutta integration to calculate the trajectories in the area where $V \neq 0$. We assume retracing, i.e. that Δ is small enough that the energy difference between electron and hole trajectory results in a separation small compared to the wavelength of the electron.

In the semiclassical description of quantum billiards with soft walls, classical turning points play an important role. They have to be accounted for in the Bohr-Sommerfeld quantization condition by a so-called Maslov index μ [31].

$$S = \oint \mathbf{p} d\mathbf{q} = 2\pi \left(n + \frac{\mu}{4} \right). \quad (3.2)$$

The value of μ depends on the dynamics at the turning point. μ is two for the reflection at a hard wall boundary, resulting in an additional phase shift of π for each bounce by an electron or hole, which gives an integer multiply of 2π in one closed Andreev loop. This is the reason we did not need to take into account a Maslov index when considering hard wall boundaries.

The reflection at a soft parabolical potential on the other hand results in a Maslov index of 1 [33], which corresponds to a phase shift of $\pi/2$. Therefore, one might think that the complete phase shift due to reflections at the soft wall boundaries must be included into the calculations, because it is no longer a multiple of 2π , as in the hard wall case. We show in Appendix A.1 that the phase contribution of the hole due to reflections at the normal conducting walls of the Andreev billiard is negative and cancels out the contribution of the electron. As a consequence, one does not need a Maslov index for the reflection at the cavity boundaries in addition to the one already included due to the reflection at the SN interface, regardless of the shape of the trajectory.

To calculate the action associated with a trajectory, consider the motion in a classical harmonic oscillator: The trapped particle travels along an ellipse in phase-space, with dimensions $a = \sqrt{E/\alpha E_F}$, $b = \sqrt{2E}$. The value of the action integral (2.25) is equal to the area of this ellipse¹. The action resulting from one reflection at the soft wall boundary is thus

$$S_{\text{refl}} = \frac{a b \cdot \pi}{2} = \frac{E\pi}{k_F \sqrt{\alpha}}. \quad (3.3)$$

¹Using the Maslov index, one can derive $E/\omega = \hbar(n + 2 \cdot 1/4)$, the factor two coming from the two reflections at both sides of the harmonic potential. Note that one obtains the exact quantum mechanical eigenvalues with this analysis.

As the above phase shift is proportional to the energy, it can be properly included in the theory by renormalizing the length of the trajectory

$$s_y \rightarrow s'_y = s_y + \frac{\pi}{\sqrt{\alpha}} \quad (3.4)$$

which leaves the formula for the semiclassical approximation to the state counting function $N_{BS}(\varepsilon)$ (2.32) unchanged. This allows us to still employ a classical $P(s')$ containing all the necessary information about the structure of the cavity.

3.0.4 Results

We want to estimate the influence different values of α will have on the agreement between the quantum mechanical state counting function and its semiclassical prediction. Due to the parabolic potential walls, the disagreement between electron and hole trajectories is increased. We give an estimate of the lateral separation y_D (see Figure (3.2)) between electron and hole trajectory after one reflection at the soft wall boundary.

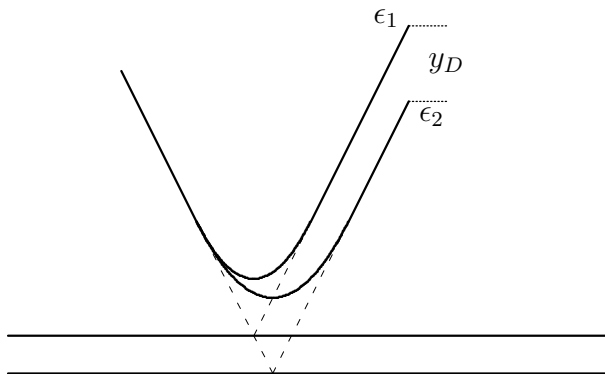


Figure 3.2: *Two particles hitting a parabolic wall with different energies $\epsilon_1 < \epsilon_2$.*

If two particles with different energies ϵ_1, ϵ_2 and some longitudinal momentum k_x hit the soft wall at the same angle, they will be reflected differently: The particle with the higher transverse velocity gets further up the slope as shown in Figure (3.2). As a result, there will be a separation between the two trajectories of

$$y_D = \frac{\pi}{k_F \sqrt{\alpha}} \delta v_y \approx \frac{\Delta}{E_F} \frac{k_F}{8\sqrt{\alpha}} \lambda_F. \quad (3.5)$$

The difference in the velocities in y direction δv_y can be roughly approximated by the difference in energies $\varepsilon/k_F \approx \Delta/2k_F$. As the soft walls are parallel to the x -axis, the separation δy between electron and hole after one complete Andreev loop will be y_D times the number of bounces at the soft walls, which we set equal to two to obtain an order of magnitude estimate.

Retracing is a good approximation if the harmonic potential is steep, i.e. $\alpha \gg 1$ and the Fermi energy small. Intuitively, this seems clear: The steeper the potential, the less time the particles spend in the $V \neq 0$ region. A lower Fermi energy means a lower number of transverse modes in the structure and therefore a lower number of reflections at the parabolic walls.

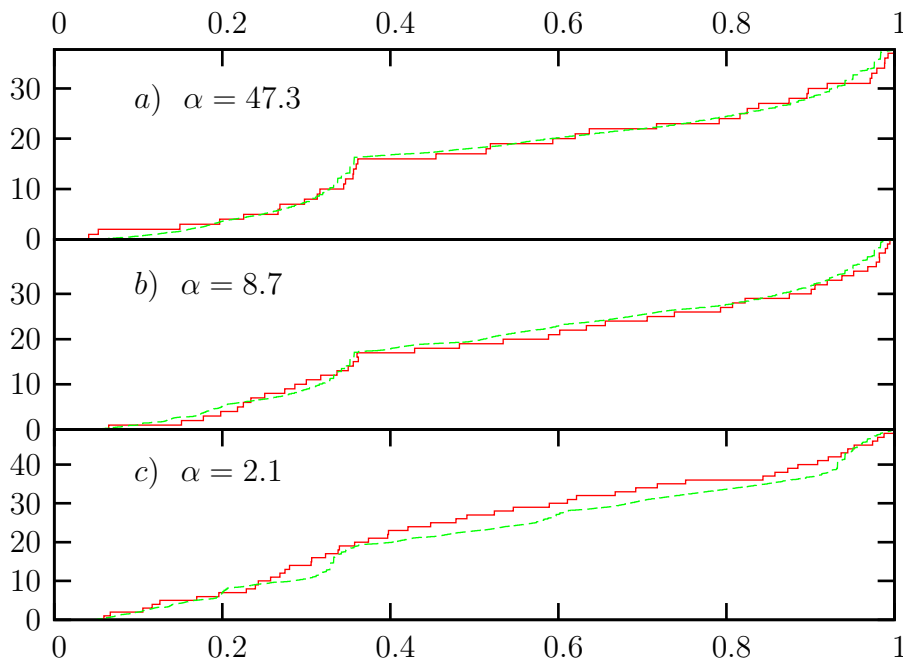


Figure 3.3: Quantum mechanical state counting function and Bohr-Sommerfeld approximation (dashed green line) for three different potential coefficients α . $W = 0.6$, $k_F = 15.5 * \pi/0.6$, $\Delta = 0.04E_F$. The root mean square deviation of the semiclassical prediction δN (see (2.38)) is 0.66, 1.15, and 8.8, $\delta y/\lambda_F \approx 0.2$, 0.6, and 1.4.(a – c)

We have tested the predictions of Equation (3.5) by looking at systems with different potential coefficients α . System *a*) presented in Figure (3.3) was calculated for a steep potential, $\alpha = 47.3$. Results show good agreement between our semiclassical approximation and the quantum results, in accordance with a low $\delta y \approx 0.2\lambda_F$. To get a more quantitative idea of the agreement between semiclassical approximation and quantum mechanics, we calculate the root mean square deviation from the quantum mechanical results defined in Equation (2.38): $\delta N = 0.9$. As α decreases, the agreement

gets worse. Figure (3.3, *b*) shows the same system as in *a* for $\alpha = 8.7$. Deviations between quantum mechanical calculations and the Semiclassical approximation appear. The biggest error seems to be in the regions between the cusps, at around $\varepsilon = 0.2\Delta$ and 0.6Δ . The reason for this is that there transverse quantization is higher, and thus the wave hits the soft wall several times, as discussed in Section 2.4.3. In Figure (3.3, *c*) $\alpha = 2.1$, $\delta y = 1.4\lambda_F$, i.e. the misplacement of the hole relative to the electron is larger than its de Broglie wavelength. As a consequence, the retracing mechanism breaks down and semiclassical approximations relying on retracing fail. No distinct cusps are visible in contrast to *a*, *b*.

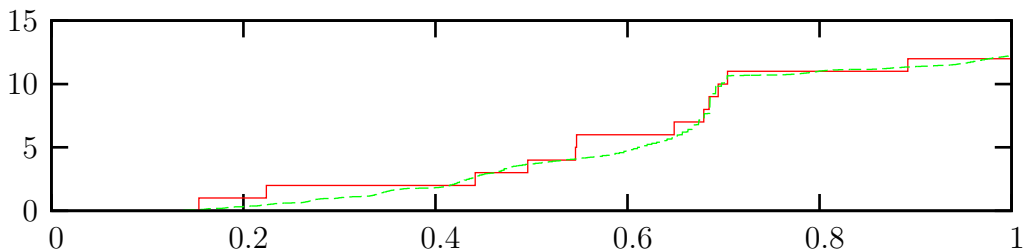


Figure 3.4: *Quantum mechanical state counting function and Bohr-Sommerfeld approximation (dashed green line) for $W = 0.6$, $\Delta = 0.02E_F$, $k_f = 10.5 * \pi/0.6$, $\alpha = 8.7$. The root mean square deviation δN is 0.66, $\delta y = 0.2\lambda_F$ as in Figure (3.3, *a*)*

Figure (3.4) shows a system with a substantially lower Fermi energy as in Figure (3.3, *b*). For the same $\alpha = 8.7$, the accuracy of the semiclassical prediction is increased in comparison to Figure (3.3, *b*), as predicted by Equation (3.5).

To determine whether indeed the absence of retracing is responsible for the large δN in (3.3, *d*), we calculated the appropriate quantum mechanical wavefunctions. Figure (3.5) shows four Andreev eigenstates of a system similar to the one in Figure (3.3,*d*). The violation of retracing can be seen by comparing electron and hole wavefunctions. The hole part of *b* shows a wavefunction that looks like an eigenstate of the closed cavity. Indeed there is such an eigenstate at the appropriate energy.

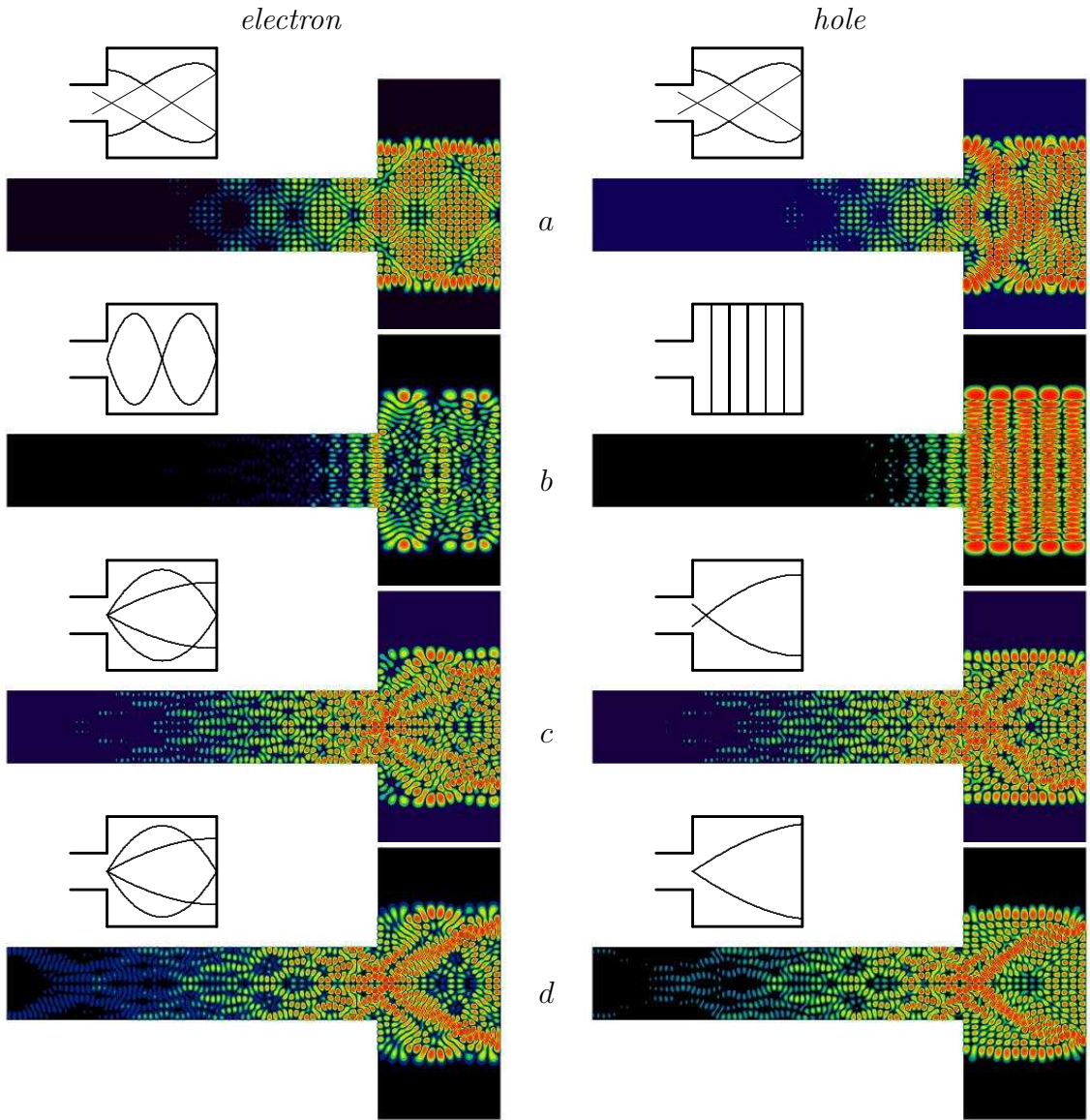


Figure 3.5: *Wavefunctions for the rectangle with soft potential walls. $k_F = 15.5\pi/0.6$, $\alpha = 2.1$, $\varepsilon = 0.27, 0.29, 0.52$ and 0.55Δ (from top to bottom). The parameters are the same as in Figure (3.3,d) apart from $\Delta = 0.02E_F$. One can see well the lengthening of the wavelength as the wavefunction climbs up the potential wall. a shows a retracing orbits. Looking at c or d however, we see that retracing is violated. While the hole trajectory hits the soft wall at the corner, the electron only hits the right wall, but makes an additional orbit.*

Chapter 4

Magnetic field

The presence of a magnetic field in an Andreev billiard is of wide spread interest [34][35][36][37]. One reason for this is that the magnetic field is easily realized as a control parameter of the experiment. From the theoretical point of view a magnetic field is interesting because it destroys retracing. The reason for this is that the hole not only has opposite charge compared to the electron, but also opposite mass and is thus equally affected by the magnetic field as the electron. For a comparison of the different quantities for electron and hole, see Figure (4). In the high magnetic field regime, the SN interface gives rise to skipping orbits with alternating electron and hole states [38], as shown in Figure (4.2).

	k	v	m	q	Equation of motion
electron	k_e	\mathbf{v}_e	m_{eff}	e	$\dot{\mathbf{v}} = e/m_{\text{eff}}(\mathbf{v} \times \mathbf{B})$
hole	$-k_e$	\mathbf{v}_e	$-m_{\text{eff}}$	$-e$	$\dot{\mathbf{v}} = e/m_{\text{eff}}(\mathbf{v} \times \mathbf{B})$

Figure 4.1: Comparison of different quantities for electron and hole. $q/m = (e/m_{\text{eff}})_e = (e/m_{\text{eff}})_h$.

We will investigate both low and high magnetic field regimes, present a semiclassical description for the low magnetic field case and discuss its limitations.

4.0.5 Implementation of a magnetic field

In the presence of a magnetic field $\mathbf{B} = B\mathbf{e}_z$, the Hamilton operator (2.5) is replaced by

$$H = \frac{1}{2m_{\text{eff}}} \left(\mathbf{p} - \frac{q}{c} \mathbf{A} \right)^2 + V(\mathbf{x}) - E_F \quad (4.1)$$

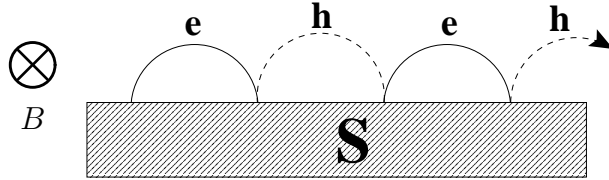


Figure 4.2: *Alternating skipping orbit on a SN boundary in a strong magnetic field perpendicular to the two dimensional structure. As electron and hole are deflected in the same direction retracing is destroyed.*

For the vector potential \mathbf{A} , satisfying $\mathbf{B} = \nabla \times \mathbf{A}$, we have in Landau gauge

$$\mathbf{A} = -y \frac{B}{c} \mathbf{e}_x. \quad (4.2)$$

According to [39], the magnetic field is incorporated into the calculation of the scattering matrix by a Peierls-phase factor in the hopping potential used to describe the coupling between adjacent gridpoints in the modular recursive Green's function method [24].

In the presence of a magnetic field, the transverse eigenfunctions of the lead $\chi_n(y) \neq \sin(k_{yn}x)$. In general, the χ_n will be a linear combination of Kummer functions. As the magnetic field destroys time reversal symmetry, there are two different transverse eigenfunctions, one for the right-moving and one for the left-moving electron or hole. This gives $2n$ linearly dependent transverse eigenstates of the lead, which fulfil a nontrivial orthogonality relation [24]. As a consequence, the simple argument in (2.2.2) by which we could use the linearly independent $\chi_n(y)$ to eliminate the sum over all modes in (2.7, 2.8) fails.

Due to the Meissner effect, the magnetic field cannot penetrate into the superconductor¹ and decays exponentially according to $B = B_0 e^{x/\lambda} \theta(-x)$, where λ is the penetration depth of the magnetic field into the superconductor [19]. However, for the exact treatment of the magnetic field in the superconductor, one has to determine the phase of the pair potential Δ correctly [40]. In Landau gauge, the pair potential is y-dependent [41]

$$\Delta(y) = \Delta_0 e^{i \operatorname{sgn}(B)y \cdot \lambda B/c} \quad (4.3)$$

¹More precisely, the magnetic field will not penetrate into the superconductor as long as it is lower than the critical field B_C in which the superconductor becomes normal conducting.

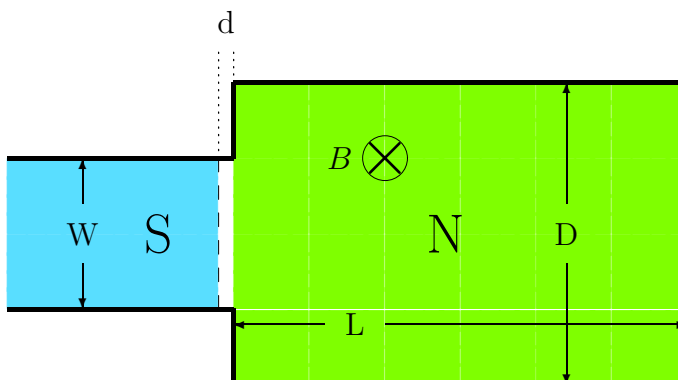


Figure 4.3: *Rectangular Andreev billiard with a perpendicular magnetic field applied B to the cavity (shaded green). $B = 0$ in the lead, which becomes superconducting after a short distance d (shaded blue). In the white normal conducting area at the junction between lead and cavity there is no magnetic field.*

The above facts make an exact inclusion of a magnetic field at the SN interface quite complicated. As our discussion of the magnetic field case focuses on the destruction of retracing properties, we consider a system where the magnetic field is set to zero inside the short normal conducting part of the lead of length d and in the superconducting region (as shown in Figure (4.3)), which allows us to continue to use Equation (2.14) while still considering the effect of a broken time reversal symmetry in the cavity. By this approach, we neglect the influence of the magnetic field on the probability of Andreev reflection [42][43]. Technically, we assume d to be very small compared to the size of the system.

4.0.6 Low magnetic field region

The low magnetic field region is characterized by nearly straight line classical trajectories, i.e. the cyclotron radius is much larger than the dimension of the cavity itself. For a semiclassical description, we can therefore neglect the curvature. Quantum mechanically, this corresponds to neglecting the diamagnetic term in (4.1)[27], which is proportional to A^2 . The low-magnetic field region is interesting because we can still attempt a semiclassical description (retracing is still valid if trajectories are straight) and we can investigate in what limits the retracing approximation is still valid.

Increasing the magnetic field from zero, the cusps in the state counting function $N(\varepsilon)$ are washed out and finally vanish. Figure (4.4) shows the position of the energy levels for different magnetic field strengths. The energy levels do not cross, due to the non-crossing-rule of Wigner and von Neumann.

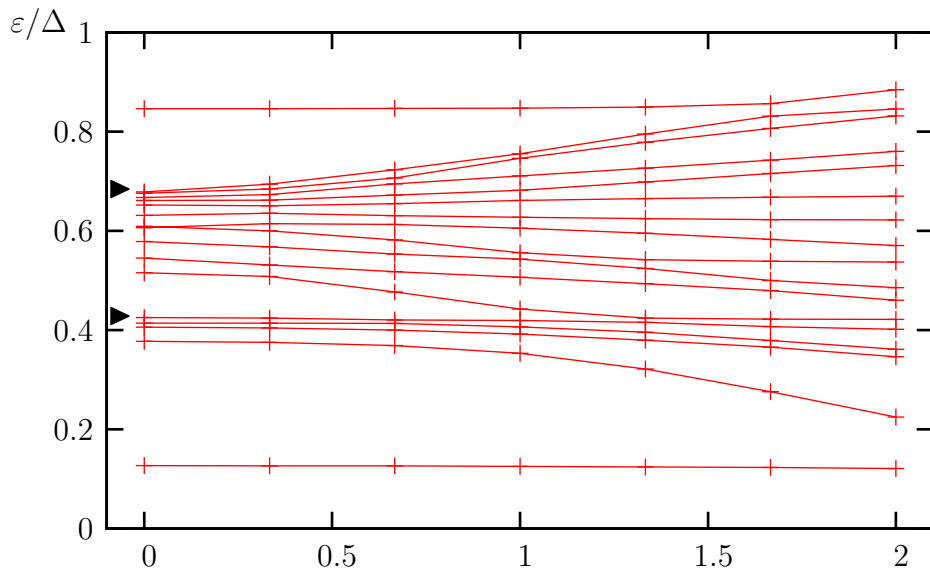


Figure 4.4: *Energies of different Andreev levels as a function of the magnetic field strength. $k_F = 15.51\pi/0.8$, $D = L = 1$. For $B/c = 0$, the cusps at $\varepsilon = 0.4\Delta$ and $\varepsilon = 0.7\Delta$ are marked by arrows. As the magnetic field increases, the energy levels spread out. For $B/c = 2$, no distinct cusp structure remains.*

While the eigenstates at the cusps are strongly affected by the magnetic field, the two energy levels at $\varepsilon = 0.85\Delta$ and $\varepsilon = 0.12\Delta$ are nearly unaffected by it. These two states correspond to bouncing ball states of the closed normal conducting billiard as shown in Figure (4.5) *a*, *c*. Their relative insensitivity with respect to B is explained by the fact that they do not enclose a finite area. The figure also shows a trajectory hitting all four sides of the cavity and thereby enclosing an area of 0.5 twice (as electron and as hole). This would give an energy shift of about

$$\delta\varepsilon \approx \frac{k_F}{s} \left(A \frac{B}{c} + \frac{\delta\varepsilon}{\Delta} \right) \rightarrow \delta\varepsilon = 0.3\Delta \quad (4.4)$$

which fits well with the numerically calculated difference in eigenenergies of 0.29Δ .

4.0.7 Semiclassical description

As we consider straight trajectories, the magnetic field enters our semiclassical description only through an Aharonov-Bohm phase $A \cdot B/c$ due to the magnetic flux enclosed by electron and hole [26]. A is the enclosed directed area of the trajectory calculated according to [29]. Note that A can be both

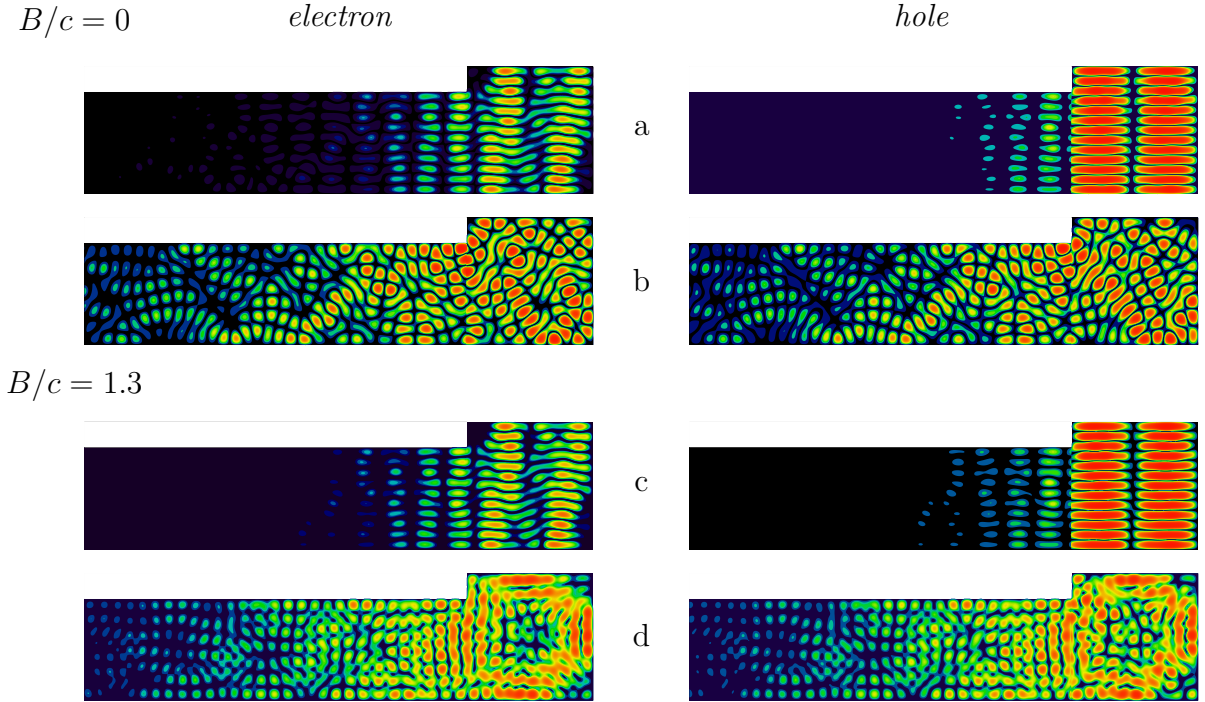


Figure 4.5: *Change of the wavefunction from zero to 1.3/c a.u. magnetic field strength. 10 open modes in the lead, $W = 0.8$. a and c show a bouncing ball state which is nearly unaffected by the magnetic field ($\varepsilon/\Delta = 0.107(a), 0.102(c)$), while the wavefunction and energy in b and d change dramatically ($\varepsilon/\Delta = 0.71(b), 0.42(d)$). Note the enclosed area in d, roughly half the size of the cavity, which is responsible for the strong magnetic field dependence of the energy.*

positive or negative depending on the orbit direction. With these considerations, Equation (2.28) changes to

$$s_n(\varepsilon, A) = \left(n\pi + A \cdot \frac{B}{c} + \arccos\left(\frac{\varepsilon}{\Delta}\right) \right) \frac{k_F}{\varepsilon}. \quad (4.5)$$

Because $s_n(\varepsilon)$ is now dependent on the enclosed area, we extend the classical pathlength distribution $P(s)$ to a joint distribution $P(s, A)$ which gives the classical probability that a trajectory entering the cavity exits after length s enclosing the area A , normalized such that $\int \int P(s, A) ds dA = 1$.

The state counting function can then be expressed according to (2.32)

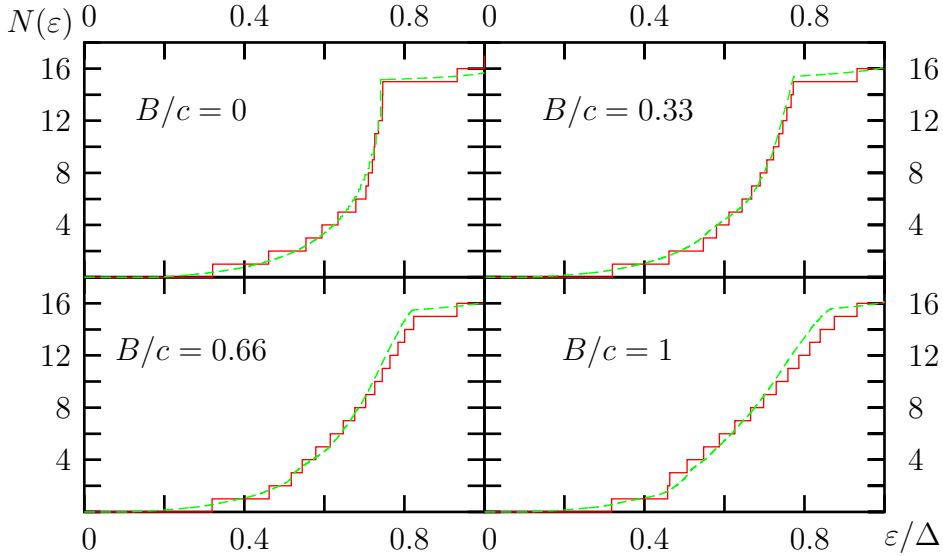


Figure 4.6: Quantum mechanical state counting function and BS-approximation (green dashed line) for $B/c = 0, 0.33, 0.66$ and 1 . The Fermi wavenumber is $k_F = 15.5\pi/1$. The misplacement of the hole relative to the electron δy due to the magnetic field is $(0., 0.38, 0.76, 1.27)\lambda_F$.

with an additional integral over all possible enclosed areas

$$N_{\text{BS}} = M \sum_{n=0}^{\infty} \int_{-\infty}^{\infty} \int_{s_n(\varepsilon, A)}^{\infty} P(s, A) ds dA. \quad (4.6)$$

We used the same Monte Carlo simulation as before to determine $P(s, A)$. Areas to a maximum of ± 0.8 a.u. were considered. Results for N_{BS} are shown in Figure (4.6). The semiclassical prediction describes the effect of the magnetic field quite well up to a field strength of $B/c \approx 0.66$. Though the qualitative picture is still quite correct for $B/c = 1$, the semiclassical approximation underestimates the spreading of the energy levels.

The cyclotron radius in atomic units is ck_F/B , in this case for $B/c = 1$ about 50, which is much larger than the size of the rectangular cavity (area $A=1$). The change in $P(s, A)$ due to the curvature of trajectories induced by the magnetic field is minimal and has no relevant effect on $N(\varepsilon)$. To better understand the discrepancies visible for $B/c = 1$, one has to explicitly look at how strongly the magnetic field affects retracing.

Considering a straight trajectory of length s connecting the SN interface with itself, we attempt to give an estimate for the width δl (see Figure (4.7))

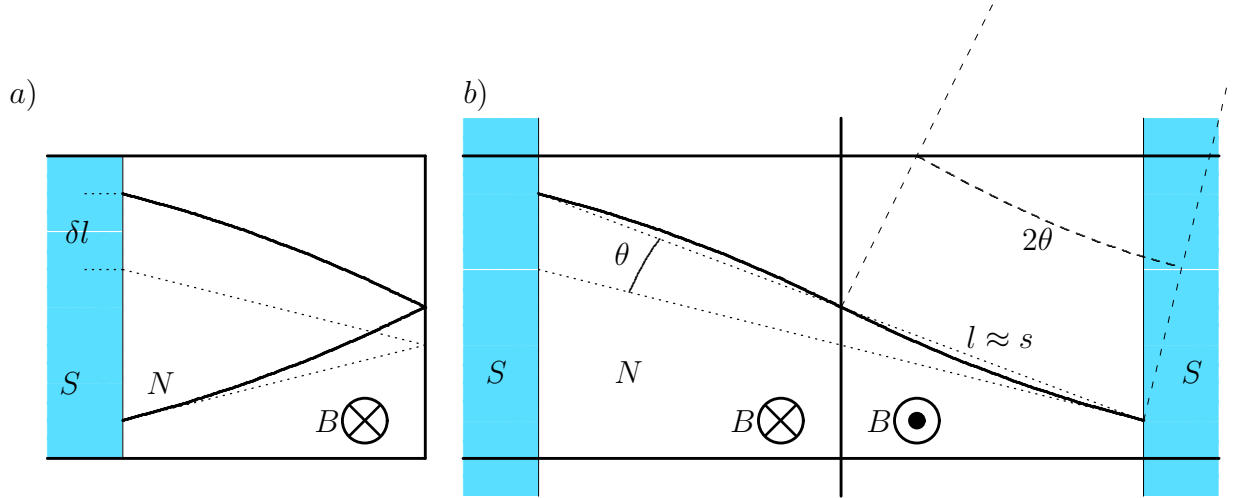


Figure 4.7: a) *Difference between a straight line and a curved trajectory in a quadratic Andreev billiard ($W = L = 1$). The classical cyclotron radius is $R = 5$. To avoid confusion, only the electron trajectory is shown. b) shows the same situation in the extended zone scheme (see Figure (2.8)). In case of a magnetic field, one has to invert the sign of the magnetic field after each reflection. The length of the trajectory $s = 4R\theta$, as needed for Equation (4.7).*

$$\delta l \approx s \sin(\theta) = s \sin\left(\frac{s}{4R}\right) \approx \frac{s^2}{4R} \quad (4.7)$$

After hitting the right wall, the trajectory curves back and hits the SN interface δl apart from a straight line trajectory. The Andreev reflected hole will be equally deflected, resulting in a total separation of $2\delta l$ in one Andreev loop. In order for retracing to stay valid, this quantity has to be small compared to the electron wavelength:

$$\frac{\delta y}{\lambda_F} = \frac{2\delta l}{\lambda_F} \approx \frac{k_F s^2}{4\pi R} = \frac{Bs^2}{4\pi c} \quad (4.8)$$

where in the last step we have used $R = ck_F/B$. Interestingly enough, $\delta y/\lambda_F$ is independent of the electron energy: The higher the Fermi energy, the larger the cyclotron radius, but the higher the resolution with which the electron “notices” that it does not arrive at the exact point the electron started from.

With this observation, we reconsider the results presented in Figure (4.6): It is not surprising that the semiclassical approximation does not yield perfect results for $B/c = 1$. At this magnetic field strength, $\delta y = 1.27\lambda_F$, which is

high enough for the electron to start noticing that retracing is no longer exact.

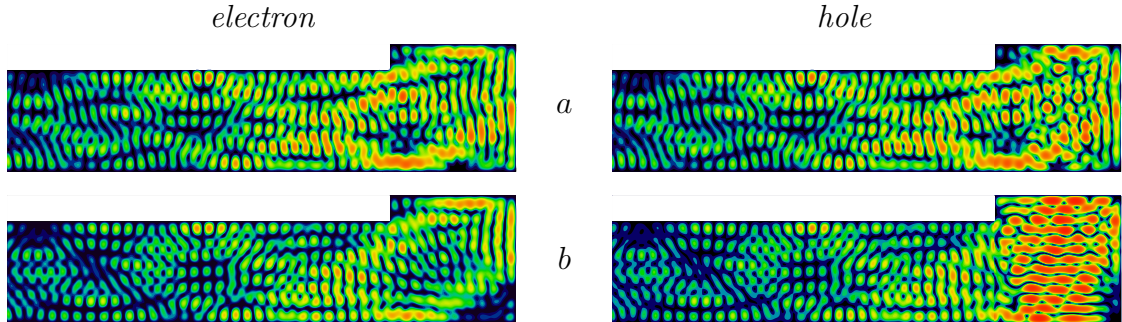


Figure 4.8: *Electron and hole wavefunction for two different magnetic field strengths (a: $B/c = 0.85$, b: $B/c = 1.3$). While the electron wavefunction (left side) is quite unaffected by the magnetic field, the hole wavefunction changes considerably. Retracing is no longer valid. $\epsilon/\Delta = 0.85(a), 0.9(b)$, system parameters see Fig. (4.5)*

The disappearance of retracing orbits with increasing strength of the magnetic field can be seen in the wavefunctions too: Figure (4.8, a) shows an Andreev state where B/c is weak enough to allow for retracing. As the magnetic field increases further, the hole wavefunction changes drastically and becomes quite dissimilar in symmetry to the electron wavefunction (see Figure (4.8, b)), as one would expect if the hole does not retrace the path of the electron. In contrast to a and c in Figure (4.5), which are dissimilar due to the excitation of an energy level of the closed normal conducting billiard near the energy $E_F - \epsilon$, this discrepancy appears with increasing magnetic field strength.

4.0.8 High magnetic field region

If the cyclotron radius is smaller than the dimensions of the cavity, we observe signatures of skipping orbits along the boundary in our wavefunctions. Figure (4.9) shows an example. Note that even though there is no retracing, and the electron and hole wavefunctions in the cavity do look different from each other, the superconducting part is very similar as demanded by the coupling in the B-dG equation. The evanescent part of the wavefunction inside the superconducting lead is very short, as $\epsilon \ll \Delta$.

In the regime of high magnetic field B , there are noticeably fewer energy levels than in the retracing regime. This becomes clear in the semiclassical picture: If retracing is operative, there is a continuum of periodic orbits,

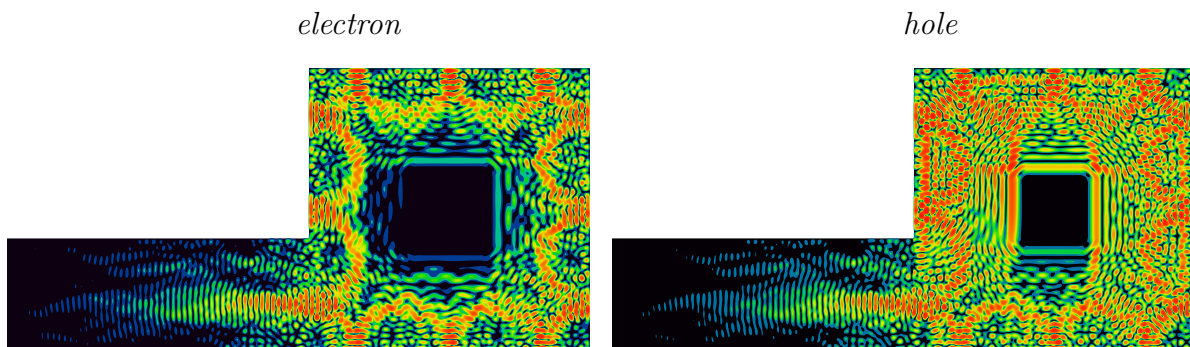


Figure 4.9: *Electron and hole moving along a skipping orbit. Both move counterclockwise along the wall. $k_F = 20.51\pi/0.4$, $B/c = 966$, $\varepsilon = 0.164\Delta$. The dimension of the cavity is 1×1 , the width of the lead $W = 0.4$, the classical cyclotron radius $= 1/6$.*

i.e. all lines connecting the SN interface with itself. As soon as retracing breaks down, only periodic orbits connecting one single point with itself are present. Figure (4.10) shows the lowest singular value of (2.14) as discussed following (2.15). A zero of this function represents an Andreev bound state. For an Andreev billiard with intact retracing, the minima are very sharp and pronounced, as shown in Figure (4.10, *a, b*). There are no minima that do not produce a zero. As soon as the process of retracing is disturbed, the energy levels start to move away from the real axis to complex values of ε . Physically this means that these eigenstates change into resonances. The figure shows all three so far discussed effects which disturb retracing, i.e. soft walls, magnetic field and narrow leads ($c - d$). Note that the change is independent of the cause of the perturbation as long as it affects retracing in a smooth way.

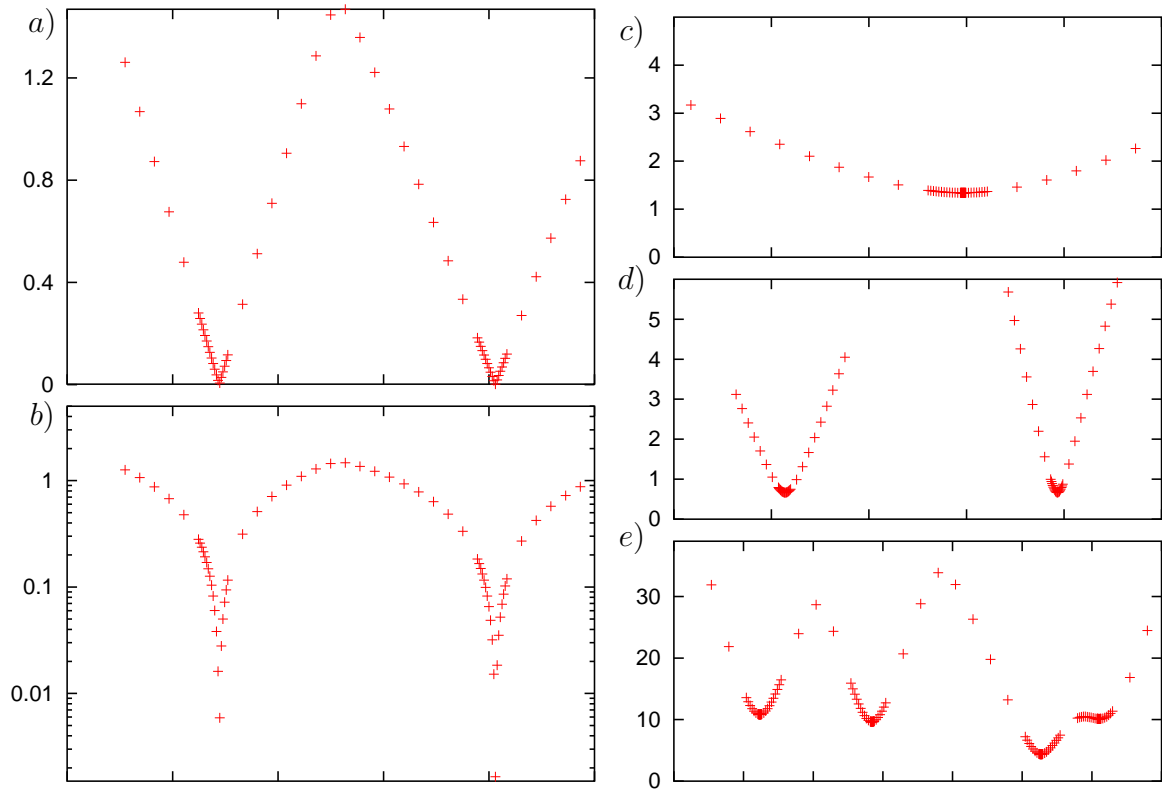


Figure 4.10: *The lowest singular value of (2.14) in arbitrary units, as a function of the excitation energy. Shown are the Andreev billiard with intact retracing, using a linear (a) and a logarithmic (b) scale. In c) the case of soft walls ($\alpha = 4$), in d) the high magnetic field case ($B/c = 600$), and in e) the narrow lead case ($w = 0.1$) for 15 open modes in the lead are shown.*

Chapter 5

Potential barrier at the SN interface

Another way of changing the role of retracing, is to reduce the probability for Andreev reflection by introducing a potential barrier at the SN interface. This case is practically very relevant since in an experiment the interface will never be perfect.

5.0.9 Quantum mechanical treatment

We model the potential barrier at the interface between a quadratic N-region and the superconducting lead by introducing a delta function at the SN interface. The corresponding potential $V(\mathbf{x}) = U_0\delta(x - x_{SN})$ enters via the wavefunction matching condition (2.13), which changes to

$$\partial_x\psi_N(x, y)|_{x=0} = \partial_x\psi_S(x, y)|_{x=0} + 2U_0\psi_S(0, y). \quad (5.1)$$

In the homogeneous matrix equation (2.14), the term $iQ^{e,h}$ is replaced by $iQ^{e,h} \mp 2iU_0\mathbf{1}$.

Figure (5.1) shows the x -dependence of a wavefunction for $\varepsilon = 0.974\Delta$. Due to the complex q_n in the exponential, the wavefunction oscillates in the superconducting region while decaying exponentially. For the Andreev eigenstate shown in the figure, the probability to find the electron in the classically forbidden region is actually higher than in the allowed region. There is no correspondence between this eigenstate and a classical orbit. As a consequence, eigenstates of this type are difficult to predict using the semiclassical techniques presented.

The probability of Andreev reflection depends on the potential barrier strength. Introducing the dimensionless barrier strength $Z = U_0/k_F$, we can

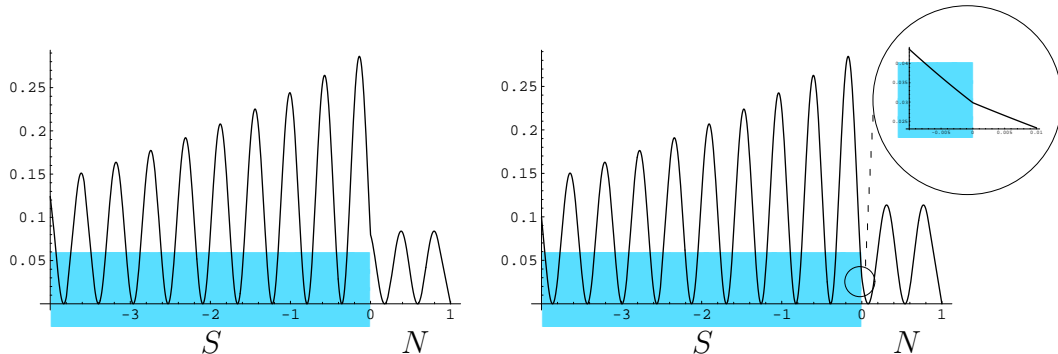


Figure 5.1: x -dependence of the electron (left) and hole (right) eigenfunction (arbitrary units) for a deltapotential of strength $U_0 = 5$, $\varepsilon = 0.974\Delta$, $k_f = 5.5\pi$, quadratic geometry with area $A = 1$, $W = 1$. The jump in the derivative of the wavefunctions due to the delta function at $x = 0$ is clearly visible. The hole wavefunction is enlarged near the SN interface.

write the probability P_A for Andreev reflection as [18]

$$P_A = \frac{\Delta^2}{\varepsilon^2 + (\Delta^2 - \varepsilon^2)(1 + 2Z^2)^2}. \quad (5.2)$$

P_A is shown in Figure (5.2). The corresponding probability for normal reflection is $P_N = 1 - P_A$. One can see in the figure that P_A reduces to 1 in the case of $Z = 0$.

Deriving a valid expression for the phase jump $\delta\phi$ is difficult. As shown in Appendix A.2,

$$\delta\phi = -\arccos\left(\frac{1}{\sqrt{1 + ((\Delta/\varepsilon)^2 - 1)(1 + 2Z^2)^2}}\right) \quad (5.3)$$

represents the phase difference between an incoming electron wave and the Andreev-reflected hole. However, if one considers an Andreev eigenstate, there will be an incoming hole wave too. For $Z = 0$, this does not influence the phase jump from electron to hole. If $Z \neq 0$ however, the phase of the outgoing hole will depend nontrivially on the phase of the incoming hole as well, because the probability for the incoming hole to be reflected normally is non zero. The same argument holds when considering an incoming hole and the Andreev reflected electron. The magnitude of the phase shift due to the reflection at a SN interface with a non-vanishing barrier is underestimated by (5.3).

As the barrier potential is smoothly switched on, the energies of the eigenstates change as shown in Figure (5.3). In contrast to the magnetic field case,

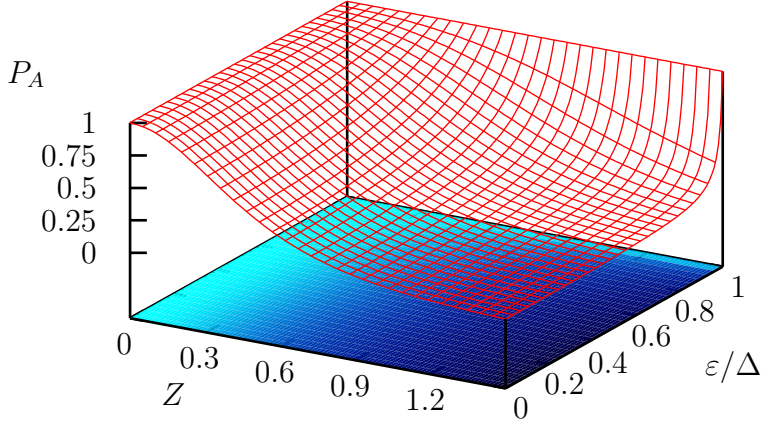


Figure 5.2: Probability for Andreev reflection P_A as a function of barrier strength Z and energy ε/Δ .

the eigenenergies do cross, because the barrier at the SN interface does not depend on y and therefore the transverse quantum number is still a “good” quantum number to discern the eigenstates. As can be seen by looking at the expression for the phase at the SN interface with a barrier (5.3), the eigenenergies should increase with increasing barrier potential: Increasing Z results in an increased value of $\delta\phi$, representing a “harder” wall. This is predicted correctly by a semiclassical approach using Equation (5.3). However the phase shift given by the quantum mechanical calculations is higher than what we expect semiclassically (not shown).

Moreover, as shown by Mortensen et al.[23], the phase shift $\delta\phi$ is dependent on the angle of incidence of the incoming electron. To describe this feature theoretically it is useful to define an effective potential strength $Z_{\text{eff}} = Z/\cos(\theta)$, where θ is the angle of incidence. $Z_{\text{eff}} \gg Z$ as θ approaches $\pi/2$. This is the reason why the eigenenergies with higher transverse quantum number in Figure (5.3) change more rapidly as a function of $Z = U_0/k_F$ than the ones situated at the cusp: The former have a higher transverse momentum, and therefore higher Z_{eff} .

While the eigenenergies situated at the cusp move slowly to higher energies as the potential increases, there are states with decreasing ε as well if one looks at Figure (5.3). They are the result of trajectories which no longer show retracing, as we will show by looking at the eigenstates.

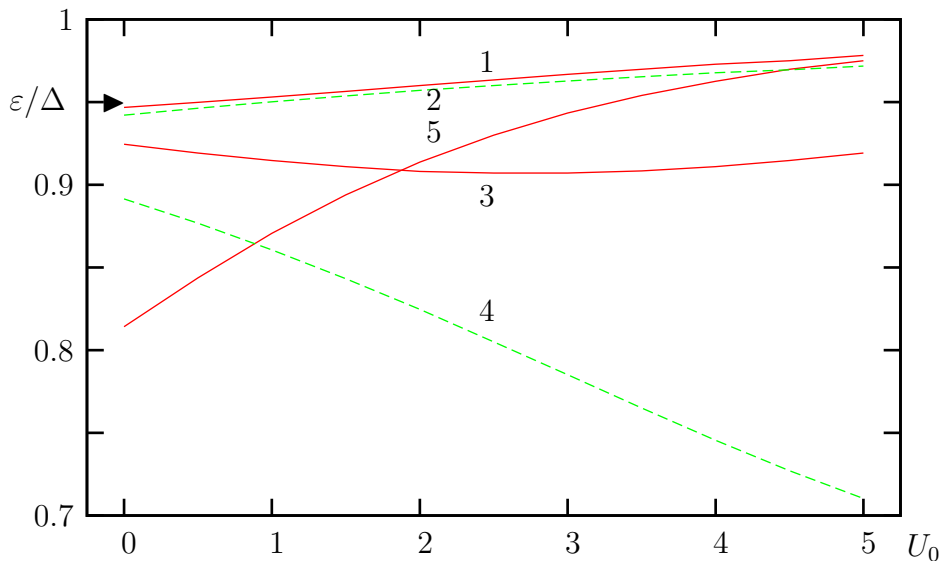


Figure 5.3: *Eigenenergies of the rectangular Andreev billiard as a function of barrier strength. There are five open modes in the quadratic cavity, $k_F = 5.5 * \pi$, $W = 1$. The transverse quantization number of each eigenstate is noted in the figure. We use dashed green lines for every other eigenenergy to make it easier to discern the different eigenstates.*

Figure (5.4) shows the quantum mechanical state counting function for different potential strengths. For low barrier strength (a and b in the figure), the general shape of $N(\varepsilon)$ looks similar to $U_0 = 0$ (compare e.g. Figure (2.10)). The only effect is a slight shift to higher energies, due to the increased phase jump at the SN interface. A cusp structure remains as the strength of the potential increases, as shown in c and d . Apart from the cusp at $\varepsilon \approx 0.85\Delta$ c shows a number of states with low energies ($\varepsilon \in [0.2, 0.6]\Delta$) which do not show retracing. As the potential increases even further, these states cease to exist, and only the cusp at $\varepsilon \approx \Delta$ remains (see Figure (5.4, d)).

Figure (5.5) shows the wavefunctions corresponding to the eigenenergies marked in Figure (5.4). State a is not part of a cusp, and there is no obvious retracing Andreev orbit visible when looking at the wavefunction. Moreover, the transverse quantum number in the rectangular cavity n_y is quite different when comparing electron ($n_y = 5$) and hole ($n_y = 11$) wavefunctions. On the other hand, $b - d$ form part of a cusp, and correspond to Andreev loops. The eigenstate d , situated directly at the cusp, looks very similar to the state shown in Figure (2.11, E). It has a transverse quantum number of

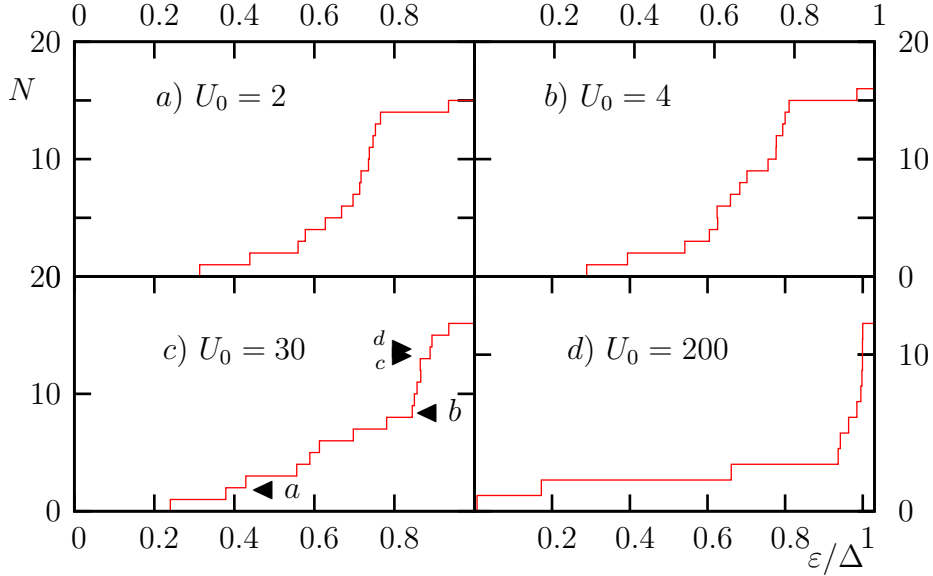


Figure 5.4: Quantum mechanical state counting function for four different barrier strengths, as shown in the insets. $k_F = 15.5\pi/W$, $W = 1(a,b)$, $0.8(c,d)$. The arrows in c) mark the energies of the wavefunctions shown in Figure (5.5).

one. Like in the $U_0 = 0$ case, if one looks at a given cusp, states with lower transverse quantum number are higher in energies. However, the slow decrease in transverse quantization, as e.g. shown in Figure (2.11), is no longer present: There is no Andreev eigenstate between c and d in Figure (5.5), in spite of the great difference in transverse quantum numbers. Note the difference in the length of the semiclassical orbits corresponding to c , $s \approx 2\sqrt{2}$ and d , $s \approx 2$, in spite of a comparatively small difference in eigenenergies. This is because of the angular dependence of Z_{eff} , which modifies the phase jump due to Andreev reflection.

It is worth noticing that even for very high barrier strength ($U_0 = 200$), a cusp situated nearly at $\varepsilon = \Delta$ remains. The probability of Andreev reflection (5.2) $P_A = 1$ near $\varepsilon \approx \Delta$ and is independent of Z as shown in Figure (5.2). This is the reason why the cusp remains so stable at high barrier strength. Non-retracing Andreev states dominate for lower ε . They do not form a distinct cusp structure, and slowly die out as the potential barrier strength increases, as can be seen by comparing c and d . The reason for this is that the probability for Andreev reflection P_A is different from zero only for $\varepsilon \approx \Delta$ for high Z as shown in Figure (5.2).

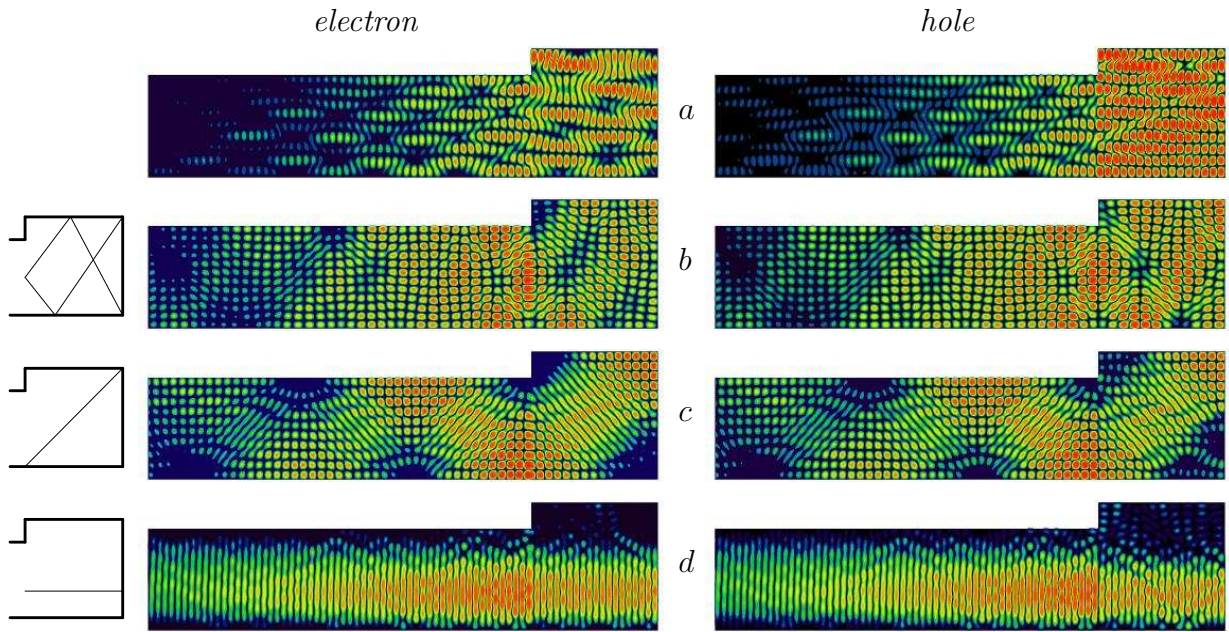


Figure 5.5: *Electron and hole wavefunction with a barrier $U_0 = 30$ at the SN interface, $k_F = 15.51\pi/0.8$. The eigenenergies corresponding to the eigenstates are marked in Figure (5.4). Eigenstate a ($\varepsilon = 0.43\Delta$) does not show retracing. The three eigenstates b – d (energies $0.855(a)$, $0.865(b)$, $0.89(c)$ in units of ε/Δ) form part of a cusp. Note the comparatively high value of the wavefunction in the classically forbidden S region, as discussed in Figure (5.1).*

Chapter 6

Summary and Outlook

In this thesis, we present a method for calculating eigenenergies and the corresponding wavefunctions of Andreev billiards. Our attention is particularly focused on billiard systems with a rectangular and a circular geometry. Using the modular recursive Green's function method allows us to calculate quantum mechanical eigenenergies and eigenfunctions with great accuracy.

These wavefunctions also yield information about retracing: By observing the change in the wavefunctions as e.g. the magnetic field increases, we can identify whether the hole still retraces the path of the electron by comparing the symmetry of electron and hole wavefunctions.

We present the semiclassical Bohr-Sommerfeld approximation using retracing and compare it to the actual quantum mechanical results. By looking directly at the quantum mechanical wavefunctions, we can identify the different paths the semiclassical approximation predicts for specific eigenenergies. Making use of a transverse quantization condition allows us to provide an approximation formula for the quantum mechanical eigenenergies.

Starting out from a rectangular model system with a wide superconducting lead, we investigate the change in dynamics as the lead becomes narrower. We find that below a certain leadwidth semiclassical approximations relying on retracing break down completely. By looking at the wavefunctions of the eigenstates of a circular Andreev billiard, we conclude that diffractive effects play an important role in the regime of narrow leads.

We investigate thoroughly the effect of non-ideal retracing conditions in an Andreev billiard: We consider a billiard with soft walls to investigate a more realistic confining potential and the effect of the Maslov index, a low magnetic field to destroy exact time reversal symmetry and a potential barrier at the SN interface to decrease the probability of Andreev reflection.

We develop a semiclassical approach for these different effects. We show that the ratio between hole displacement and de Broglie wavelength of the

electron is an indicator for how good the retracing approximation is. This allows us to predict the point where semiclassical approximations relying on retracing fail to predict quantum mechanics.

By looking at the determinantal equation for the eigenenergies in an Andreev billiard, we can see the movement of the eigenenergies away from the real axis. Physically this means that the eigenstates change into resonances. We find that this behaviour is independent of the type of the effect responsible for the absence of retracing, as long as the hole displacement δy is smoothly dependent on the perturbation.

The methods presented in this thesis are suitable to investigate other geometries for the Andreev billiard. A very interesting case would be a chaotic cavity, e.g. a Bunimovich stadium. This structure exhibits chaotic dynamics in the normal-conducting state. By bringing it in contact with a superconductor, a new class of periodic orbits is created, giving rise to regular dynamics.

Another topic we have not discussed is the semiclassical description of Andreev billiards without relying on retracing and the Bohr-Sommerfeld quantization rule. Using this approach it would be possible to investigate Andreev billiards in e.g. a high magnetic field semiclassically.

By using open structures with more than one lead, one can investigate either billiards in contact with two superconductors or transport through an Andreev billiard. The former would allow to introduce a phase difference in the two pair potentials. The latter makes the Andreev billiard accessible to quantum transport investigations.

Appendix A

Derivation of SN reflection phase

A.1 Clean SN interface

We first investigate the scattering at a clean SN interface. The SN interface is situated at $x_{\text{SN}} = 0$, the superconductor extends in negative x direction. Using the same approach as in [18], we make the ansatz of an

$$\begin{aligned}\psi_N &= (e^{-ik_e x} + ae^{ik_e x}) \begin{pmatrix} 1 \\ 0 \end{pmatrix} + be^{-ik_h x} \begin{pmatrix} 0 \\ 1 \end{pmatrix} \\ \psi_S &= ce^{-iq^- x} \begin{pmatrix} \gamma \\ 1 \end{pmatrix} + de^{iq^+ x} \begin{pmatrix} \gamma^* \\ 1 \end{pmatrix}.\end{aligned}\tag{A-1}$$

In order for ψ_S to be an eigenfunction of the B-dG equation (2.4), $\gamma = \Delta/(\varepsilon + i\sqrt{\Delta^2 - \varepsilon^2})$, $|\gamma|^2 = 1$. The coefficient $|a|^2$ gives the probability for normal reflection, $|b|^2$ the one for Andreev reflection. We insert the ansatz (A-1) into the wave function matching conditions (2.12) and (2.13). To simplify the calculations, we assume $k_{e,h} \approx q^\pm \approx k_F$.

$$\begin{aligned}\psi_N(0) = \psi_S(0) &: \\ 1 + a &= \gamma c + \gamma^* d\end{aligned}\tag{A-2}$$

$$b = c + d\tag{A-3}$$

$$\begin{aligned}\partial_x \psi_N(x)|_{x=0} = \partial_x \psi_S(x)|_{x=0} &: \\ -1 + a &= -\gamma c + \gamma^* d\end{aligned}\tag{A-4}$$

$$-b = -c + d\tag{A-5}$$

The solution of the above system of equations is $a = d = 0$, $b = c = 1/\gamma$. The phase difference between incoming electron and Andreev reflected hole

is the phase of b ,

$$\arg(b) = -\arg(\gamma) = -\arccos\left(\frac{\operatorname{Re}(\gamma)}{|\gamma|^2}\right) = -\arccos(\varepsilon/\Delta) \quad (\text{A-6})$$

which is used in (2.6).

Now we want to show that the phase jump of the hole which is Andreev reflected into an electron makes another contribution of (A-6). After being reflected inside the cavity, the hole returns with a negative sign in the exponent. This corresponds to the same calculation as for the electron using the ansatz

$$\psi_N = (e^{ik_h x} + a e^{-ik_h x}) \begin{pmatrix} 0 \\ 1 \end{pmatrix} + b e^{ik_e x} \begin{pmatrix} 1 \\ 0 \end{pmatrix} \quad (\text{A-7})$$

which yields exactly the same result for the argument of b as in (A-6) (not the negative one). From this, it follows that the two phase jumps due to Andreev reflection indeed add up to a total of two times (A-6) in one Andreev loop. This is in contrast to phase jumps due to reflections at normal conducting walls inside the cavity. Consider for example an electron wave hitting a potential barrier of finite height $V = V_0 \theta(x)$ situated at $x = 0$. If the height of the potential is higher than the energy of the incident electron E , it will be reflected back. Inserting into a one dimensional Schrödinger equation the ansatz

$$\psi = (e^{ikx} + a_e e^{-ikx}) \theta(-x) + b_e e^{\kappa x} \theta(x), \quad k = \sqrt{2E}, \quad \kappa = \sqrt{2(V_0 - E)} \quad (\text{A-8})$$

we obtain the coefficient of the reflected wave as

$$a_e = \frac{\kappa^2 - k^2 + 2i\kappa k}{\kappa^2 + k^2}. \quad (\text{A-9})$$

The magnitude $|a_e| = 1$. The sign of the imaginary part of a , and thereby the sign of the phase $\arg(a_e)$, depends on the sign of k . A hole moving in the same direction as the electron is described by the ansatz

$$\psi = (e^{-ikx} + a_h e^{ikx}) \theta(-x) + b_h e^{\kappa x} \theta(x). \quad (\text{A-10})$$

The coefficients a_e and a_h are related by $a_e = a_h^*$. As a consequence, $\arg(a_e) = -\arg(a_h)$. For a harmonic potential, the calculations are more difficult, but the result is the same. In contrast to Andreev reflection, the total phase contribution due to a reflection at a normal conducting parabolic wall in an Andreev loop is thus $\arg(a_e) + \arg(a_h) = 0$.

A.2 Potential barrier at the SN interface

Finally, we look at what happens if a barrier of strength $U_0 = k_F \cdot Z$ at the SN interface is present. In this case, we insert the ansatz of Equation (A-1) into the matching conditions (2.12) and (5.1). After making the same approximations as in A.1, we obtain the result

$$b = \frac{1}{\gamma + 2Z^2 \text{Im}\gamma} \quad (\text{A-11})$$

$$\begin{aligned} \arg(b) &= -\arg(\gamma + 2iZ^2 \text{Im}\gamma) \\ &= -\arccos\left(\frac{\text{Re}\gamma}{|\gamma + 2iZ^2 \text{Im}\gamma|}\right) \\ &= -\arccos\left(\frac{1}{\sqrt{1 + ((\Delta/\varepsilon)^2 - 1)(2Z^2 + 1)^2}}\right). \end{aligned} \quad (\text{A-12})$$

In the case of $Z=0$, this simplifies to (A-6).

However, the above formula is no longer true if one uses the more general ansatz of an incoming electron and hole, which have a phase difference $\delta\phi$

$$\psi_N = (e^{ik_\epsilon x} + ae^{ik_\epsilon x}) \begin{pmatrix} 1 \\ 0 \end{pmatrix} + (e^{i\delta\phi} e^{ik_h x} + be^{-ik_h x}) \begin{pmatrix} 0 \\ 1 \end{pmatrix}. \quad (\text{A-13})$$

In this case, b consists of contributions from an Andreev reflected electron and a normal reflected hole.

$$b = -\frac{1 + 2Z(i + Z)\text{Im}\gamma e^{i\delta\phi}}{2Z^2 \text{Im}\gamma - \gamma^*} \quad (\text{A-14})$$

The phase $\delta\phi$ shows up in the numerator of b . As a consequence, the phase of b depends nontrivially on $\delta\phi$, which cannot be known without solving the quantum mechanical problem for a particular trajectory.

From this we conclude that it is not possible to give as general a formula as (A-6) for the Maslov index of an SN interface with a barrier present.

Appendix B

Semiclassical eigenenergies

We will try increase the accuracy of the formula presented in Equation (2.35) further. We start out from the transverse quantization condition for k_{ym}

$$k_{ym} = \frac{m * \pi}{W}. \quad (\text{B-1})$$

We do not make the Taylor expansion in calculating the action integral (2.26)

$$S = s(k_e - k_h) = s\sqrt{2} \left(\sqrt{E_F - \varepsilon} + \sqrt{E_F + \varepsilon} \right). \quad (\text{B-2})$$

To shorten the notation, we define $k_{e,h}^2 = 2(E_F \pm \varepsilon)$. To take into account the difference in length between electron and hole trajectory, we split up their contributions

$$s = \frac{s_e + s_h}{2} = L \left(\frac{1}{\cos(\theta_e)} + \frac{1}{\cos(\theta_h)} \right). \quad (\text{B-3})$$

For the definitiopn of θ , see Figure (2.8). We now discern between electron and hole angle. Both can be expressed using the wavenumbers:

$$\sin(\theta_{e,h}) = \frac{k_{ym}}{k_{e,h}} \quad (\text{B-4})$$

Now we use the more accurate Equation (B-3) for the path length s in (B-2). According to Equation (2.28), we insert the Maslov index $\arccos(\frac{\varepsilon}{\Delta})$ of the reflection at the SN interface. Finally, we arrive at

$$\frac{k_FL}{2} (k_e - k_h) \left(\frac{k_e}{\sqrt{k_e^2 - k_{my}^2}} + \frac{k_h}{\sqrt{k_h^2 - k_{my}^2}} \right) = n\pi + \arccos(\varepsilon/\Delta). \quad (\text{B-5})$$

which was used to determine the eigenenergies in (2.12).

Bibliography

- [1] C.M. Marcus, A.J. Rimberg, R.M. Westervelt, P.F. Hopkins, and A.C. Gossard. Conductance fluctuations and chaotic scattering in ballistic microstructures. *Phys.Rev.Lett.*, 69(506), 1992.
- [2] I.V. Zozoulenko, R. Schuster, K. F. Berggren, and K. Ensslin. Ballistic electrons in an open square geometry: Selective probing of resonant-energy states. *Phys.Rev.B*, 55(10209), 1997.
- [3] O.Bohigas, M.Giannoni, and C.Schmit. Characterization of chaotic quantum spectra and universality of level fluctuation laws. *Phys.Rev.Lett.*, 52(1), 1984.
- [4] E.Heller. Bound-state eigenfunctions of classically chaotic hamiltonian systems: Scars of periodic orbits. *Phys.Rev.Lett*, 53(1515), 1984.
- [5] D.K. Ferry and S.M. Goodwick. *Transport in Nanostructures*. Cambridge University Press, 1999.
- [6] J.Davies. *The physics of low-dimensional semiconductors*. Cambridge University press, 1998.
- [7] J.Bardeen, L.Cooper, and J.Schrieffer. Theory of superconductivity. *Phys.Rev.Lett.*, 108(1175), 1957.
- [8] H.Vogel. *Physik*. Springer-Verlag Berlin, 1995.
- [9] J.Cserti, A.Bondor, J.Koltai, and G.Vattay. Excitation spectra for Andreev billiards of box and disk geometries. *Phys.Rev.B*, 66(064528), 2002.
- [10] H.Schomerus and C.Beenakker. Excitation spectrum of Andreev billiards with a mixed phase space. *Phys.Rev.Lett*, 82(2951), 1999.
- [11] A.Altland and M.Zirnbauer. Random matrix theory of a chaotic Andreev quantum dot. *Phys.Rev.Lett*, 76(3420), 1996.

- [12] J.A.Melsen, P.W.Brouwer, K.M. Frahm, and C.W.J. Beenakker. Induced superconductivity distinguishes chaotic from integrable billiards. *Europhys.Lett.*, 35(7), 1996.
- [13] A.Lodder and Y.Nazarov. Density of states and the energy gap in andreev billiards. *Phys.Rev.B*, 58(5783), 1998.
- [14] A.Kormanyos, Z.Kaufmann, J.Cserti, and C.J.Lambert. A logarithmic contribution to the density of states of rectangular Andreev billiards. *Phys.Rev.B*, 67(172506), 2003.
- [15] J.Cserti, A.Kormanyos, Z.Kaufmann, and J.Koltai. Proximity-induced supgaps in Andreev billiards. *Phys.Rev.Lett*, 89(057001), 2002.
- [16] S. Rotter, J. Burgdörfer, L. Wirtz, J. Tang, and J. Trost. A modular recursive Green's function method for quantum transport. *Phys.Rev.B*, 62(1950), 2000.
- [17] R.Enderlein and N. Horing. *Fundamentals of Semiconductor Physics and Devices*. World Scientific, 1997.
- [18] G.Blonder, M.Tinkham, and T.Klapwijk. Transition from metallic to tunneling regimes in superconducting microconstrictions: Excess current, charge imbalance and supercurrent conversion. *Phys.Rev.B*, 4515(7), 1982.
- [19] H.Weber and O.Hittmair. *Supraleitung*. Verlag Karl Thieme München, 1979.
- [20] C.W.J.Beenakker. Random-matrix theory of quantum transport. *Rev.Mod.Phys.*, 69(731), 1997.
- [21] P.De Gennes. *Superconductivity of Metals and Alloys*. Benjamin, New York, 1966.
- [22] A.Andreev. The thermal conductivity of the intermediate state in superconductors. *Sov.Phys.JETP*, 19(1228), 1964.
- [23] N.Mortensen, K.Flensberg, and A. Jauho. Angle dependence of andreev scattering at semiconductor-superconductor interfaces. *Phys.Rev.B*, 59(15), 1999.
- [24] S. Rotter, B. Weingartner, N. Rohringer, and J. Burgdörfer. Ballistic quantum transport at high energies and high magnetic fields. *Phys.Rev.B*, 68(165302), 2003.

- [25] H.U. Baranger and A.D. Stone. Electrical linear-response theory in an arbitrary magnetic field: A new Fermi-surface formation. *Phys.Rev.B*, 40(8169), 1989.
- [26] W.Ihra, M.Leadbeater, J.Vega, and K.Richter. Semiclassical theory of integrable and rough Andreev billiards. *Eur.Phys.J.B.*, 21(425), 2001.
- [27] L.Wirtz, J.Tang, and J.Burgdörfer. Gauge-invariant theory for semiclassical magnetotransport through ballistic microstructures. *Phys.Rev.B.*, 59(2956), 1999.
- [28] L.Wirtz, C.Stampfer, S.Rotter, and J.Burgdörfer. Semiclassical theory for transmission through open billiards: Convergence towards quantum transport. *Phys.Rev.E*, 67(016206), 2003.
- [29] L. Wirtz. Semiclassical scattering in mesoscopic ballistic semiconductor devices. Master's thesis, University of Tennessee, 1997.
- [30] A.Messiah. *Quantum mechanics*. North Holland publishing company, 1968.
- [31] M.Brack and R.Bhaduri. *Semiclassical physics*. Addison Wesley Publishing Company, 1997.
- [32] Bernhard Weingartner. Electron transport through a quantum dot with mixed classical dynamics. Master's thesis, Vienna University of Technology, 2004.
- [33] D.A.Goodings and N.D.Whelan. Bogomolny's semiclassical transfer operator for rotationally invariant integrable systems. *J.Phys.A*, 31(7521), 1998.
- [34] Y.Takagaki and K.Ploog. Conductance fluctuations of semiconductor-superconductor microjunctions in the quantum Hall regime. *Phys.Rev.B*, 58(7162), 1998.
- [35] T.Moore and D.Williams. Andreev reflection at high magnetic fields. *Phys.Rev.B.*, 59(11), 1999.
- [36] I.Kosztin, D.Maslov, and P.Goldbart. Chaos in Andreev billiards. *Phys.Rev.Lett.*, 75(1735), 1995.
- [37] J. Wiersig. Pseudointegrable Andreev billiard. *Phys.Rev.E*, 65(036221), 2002.

- [38] J.Cserti, P.Polinak, G.Palla, U.Zülicke, and C.J.Lambert. Ring-shaped Andreev billiards in quantizing magnetic fields. *Phys. Rev. B*, 69(134514), 2004.
- [39] R.E. Peierls. Zur Theorie des Diamagnetismus von Leitungselektronen. *Z.Phys.*, 80, 1933.
- [40] T.Antsygina, E.Bratus, and A.Svidzinskii. Josephson current in a SNS contact in the presence of a magnetic field. *Sov.J.Low Temp.Phys.*, 1(49), 1974.
- [41] H.Hoppe, U.Zülicke, and G.Schön. Andreev reflection in strong magnetic fields. *Phys.Rev.Lett*, 84(8), 2000.
- [42] G.Tkachov and V.Fal'ko. Magnetic field influence on the proximity effect in semiconductor-superconductor hybrid structures and their thermal conductance. *Phys.Rev.B*, 69(092503), 2004.
- [43] J.Eroms, M.Tolkiehn, D.Weiss, U.Rössler, J.Boeck, D.Jo, and S.Borghs. Chaotic motion and suppressiopn of commensurability effects in an andreev antidot billiard. *Physica E*, 12(918), 2002.

Acknowledgements

At this point, I would like to thank the people who made this work possible, and helped me on the way:

- My thesis advisor Prof.Dr. Joachim Burgdörfer for his guidance, ideas, and many fruitful discussions.
- My co-advisor Dr. Stefan Rotter for encouragement, suggestions and always finding time for every question. And for teaching me to listen to music while I work.
- Prof.Dr. Jozsef Cserti and Dr. Andor Kormanyos for their hospitality, explanations, and ideas.
- Dr. Christoph Lemell, for solving computer problems and showing me how to optimize my code.
- DI Bernhard Weingartner and Florian Aigner for many comments, suggestions and difficult questions.
- All the other colleagues in the group of Prof. J. Burgdörfer at the Institute for Theoretical Physics at the Technical University of Vienna for many interesting conversations.

The numerical calculations were performed on computers of the Zentraler Informatikdienst der TU Wien.

Last but not least, I would like to thank my parents and my friends for their support during my studies.